SYNTHESIS AND CHARACTERISATION OF ZINC OXIDE NANOPARTICLES USING PEPPERMINT TEA (*Mentha piperita*) DREGS EXTRACT AND THEIR PHOTOCATALYTIC PERFORMANCE

By

LOH XUE LIN

A project report submitted to the Department of Chemical Science

Faculty of Science

Universiti Tunku Abdul Rahman

in partial fulfilment of the requirements for the degree of

Bachelor of Science (Hons) Chemistry

May 2022

ABSTRACT

SYNTHESIS AND CHARACTERISATION OF ZINC OXIDE NANOPARTICLES USING PEPPERMINT TEA (*Mentha piperita*) DREGS EXTRACT AND THEIR PHOTOCATALYTIC PERFORMANCE

LOH XUE LIN

Nanoparticles are classified as materials with a scale ranging from 1-100 nm. Nanoparticles are of profound scientific interest because they span the gap between bulk materials and atomic or molecular structures. Zinc oxide is a n-type semiconductor with a wide band gap of 3.37 eV and a large excitation binding energy of 60 meV. It is widely used in electronics, optoelectronics and laser technology. Zinc oxide nanoparticles is considered as one of the best photocatalyst for the degradation of pollutants in water since it has large surface area that enhances the photocatalytic activity. The aim of this project is to study the possibility of using peppermint tea dregs extract as the agricultural waste with zinc nitrate hexahydrate as salt precursor to synthesise zinc oxide nanoparticles through a simple, low cost, greener and environmentally friendly pathway. The qualitative phytochemical screening of peppermint tea dregs extract revealed the presence of flavonoids which can be served as the reducing agent and stabilising agent in the synthesis of zinc oxide nanoparticles. In addition, the effects of mass of zinc nitrate hexahydrate used and calcination

temperature on the synthesis of zinc oxide nanoparticles were also studied. The synthesised zinc oxide nanoparticles were characterised via various analytical techniques such as Fourier transform infrared spectroscopy (FTIR), ultraviolet-visible spectroscopy (UV-Vis), X-ray diffraction (XRD), field emission scanning electron microscopy (FESEM), energy dispersive X-ray analysis (EDX) and particle size analysis (PSA). The photocatalytic performance of zinc oxide nanoparticles synthesised was evaluated by the degradation of crystal violet dye in aqueous solution with exposure to sunlight. The extent of dye degradation was monitored by using UV-Vis spectrophotometer.

ABSTRAK

SINTESIS DAN PENCIRIAN NANOPARTIKEL ZINK OKSIDA DENGAN MENGGUNAKAN EKSTRAK HAMPAS TEH PUDINA (*Mentha piperita*) DAN PRESTASI FOTOKATALITIK-NYA

LOH XUE LIN

Nanopartikel dikelaskan sebagai sejenis bahan dengan skala 1-100 nm. Nanopartikel mendapati minat saintifik yang mendalam kerana pencirian pada skala nanometer adalah jauh berbeza daripada sifat pukal makroskopiknya. Zink oksida merupakan n-jenis semikonduktor yang terkenal dengan jurang jalur 3.37 eV dan tenaga ikatan teruja 60 meV. Ia telah digunakan secara meluas dalam sektor elektronik, optoelektronik dan teknologi laser. Oleh itu, nanopartikel zink oksida dianggap sebagai salah satu fotokatalis yang terbaik bagi degradasi bahan pencemaran dalam air buangan kerana ia mempunyai luas permukaan yang besar dan dapat mempertingkatkan aktiviti fotokatalitik. Misi projek ini adalah untuk mengaji potensi sintesis nanopartikel zink oksida dengan menggunakan ekstrak hampas teh pudina sebagai sisa pertanian dan zink nitrat heksahidrat sebagai pendahulu melalui laluan yang mudah, kos rendah, hijau dan mesra alam. Pemeriksaaan fitokimia bagi ekstrak hampas teh pudina telah mengesankan kehadiran flavonoids yang boleh memainkan peranannya sebagai agen penurunan dan agen penstabil dalam sinthesis nanopartikel zink oksida. Bukan itu sahaja, kesan-kesan daripada keberatan zink nitrat heksahidrat dan suhu

kalsinasi dalam sinthesis nanopartikel zink oksida juga dikajikan. Pencirian nanopartikel zink oksida yang dihasil telah dikenalpastikan melalui pelbagai kaedah analisis seperti spektroskopi inframerah Fourier transformasi (FTIR), spektroskopi ultraviolet-vis (UV-Vis), difraksi sinar-X (XRD), mikroskop elektron pengimbasan pelepasan medan (FESEM), analisis penyebaran tenaga sinar-X (EDX) dan penganalisis saiz zarah (PSA). Prestasi fotokatalitik nanopartikel zink oksida telah dinilai melalui degradasi pewarna crystal violet dalam larutan akueus dengan penyinaran cahaya matahari. Tahap degradasi pewarna telah dipantau dengan menggunakan spektroskopi ultraviolet-vis (UV-Vis).

ACKNOWLEDGEMENTS

First of all, I would like to express my deepest appreciation to my supervisor, Dr. Ooi Zhong Xian for his valuable assistance, advice, guidance and support throughout my final year project. It is a great honour to work under his supervision. His regular advice and suggestions have made my work easier and proficient.

Furthermore, I would like to express my sincere gratitude to Universiti Tunku Abdul Rahman (UTAR) for offering me an opportunity to complete my research project by providing all the equipment and facilities.

Moreover, I own my heartfelt gratitude to the laboratory staffs especially Mr. Goh Wee Sheng, Mr. Seou Chi Kien and Mr. Ooh Keng Fei who shared me a lot of knowledges and allocated their precious time to teach me the appropriate techniques in the operation of equipment as well as assisted me to analyse my synthesized products using FTIR, UV-Vis, XRD, SEM, EDX and PSA.

Last but not least, a special word of thanks goes to my family and friends for their unconditional encouragement, love and support throughout this entire research project.

DECLARATION

I hereby declare that this final year project report is based on my original work except for quotations and citations which have been duly acknowledged. I also declare that it has not been previously or concurrently submitted for any other degree at UTAR or other institutions.

LOH XUE LIN

APPROVAL SHEET

This final year project report entitled "**SYNTHESIS AND CHARACTERISATION OF ZINC OXIDE NANOPARTICLES USING PEPPERMINT TEA (*Mentha piperita*) DREGS EXTRACT AND THEIR PHOTOCATALYTIC PERFORMANCE**" was prepared by LOH XUE LIN and submitted as partial fulfilment of the requirements for the degree of Bachelor of Science (Hons) Chemistry at Universiti Tunku Abdul Rahman.

Approved by:

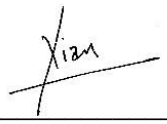

Date: 01 June 2022

(Asst. Prof. Dr. Ooi Zhong Xian)

Supervisor

Department of Chemical Science

Faculty of Science

Universiti Tunku Abdul Rahman

FACULTY OF SCIENCE

UNIVERSITI TUNKU ABDUL RAHMAN

Date : 01 June 2022

PERMISSION SHEET

It is hereby certified that **LOH XUE LIN** (ID No: **19ADB04060**) has completed this final year project report entitled "SYNTHESIS AND CHARACTERISATION OF ZINC OXIDE NANOPARTICLES USING PEPPERMINT TEA (*Mentha piperita*) DREGS EXTRACT AND THEIR PHOTOCATALYTIC PERFORMANCE" under the supervision of Asst. Prof. Dr. Ooi Zhong Xian from the Department of Chemical Science, Faculty of Science.

I hereby give permission to the University to upload the softcopy of my final year project report in pdf format into the UTAR Institutional Repository, which may be made accessible to the UTAR community and public.

Yours truly,

_____

(LOH XUE LIN)

TABLE OF CONTENTS

LIST OF TABLES

LIST OF FIGURES

LIST OF ABBREVIATIONS

CH_3COOH	Acetic acid
AFM	Atomic force microscope
BPB	Bromo phenol blue
CO_2	Carbon dioxide
CV	Crystal violet
e_{cb}^-	Electron of conduction band
EDX	Energy dispersive X-ray analysis
$FeCl_2$	Ferric(II) chloride
$FeCl_3$	Ferric(III) chloride
FESEM	Field emission scanning electron microscopy
FTIR	Fourier transform infrared spectroscopy
FWHM	Full width at half maximum
GC-MS	Gas chromatography-mass spectrometry
h^+	Hole
h_{vb}^+	Hole of valence band
HCl	Hydrochloric acid
H^+	Hydrogen ion
H_2O_2	Hydrogen peroxide
HOO•	Hydroperoxyl radical
OH^-	Hydroxide ion
OH•	Hydroxyl radical
ICDD	International Centre for Diffraction Data
$Pb(CH_3COO)_2$	Lead acetate

LC-MS	Liquid chromatography-mass spectrometry
MB	Methylene blue
HNO_3	Nitric acid
O	Oxygen
PSA	Particle size analysis
PSD	Particle size distribution
KBr	Potassium bromide
SEM	Scanning electron microscopy
STM	Scanning tunnelling microscope
NaOH	Sodium hydroxide
H_2SO_4	Sulphuric acid
$O•_2^-$	Superoxide radical
TEM	Transmission electron microscopy
UV-Vis	Ultraviolet-visible spectroscopy
H_2O	Water
λ	Wavelength
XRD	X-ray diffraction
Zn	Zinc
$Zn(OH)_2$	Zinc hydroxide
$Zn(NO_3)_2.6H_2O$	Zinc nitrate hexahydrate
ZnO	Zinc oxide
ZnO NPs	Zinc oxide nanoparticles

CHAPTER 1

INTRODUCTION

1.1 Nanotechnology and Nanoparticles

Nanotechnology has created several prospects for advancement in the fields of technology and science, owing to its capacity to manipulate metals into nanoscales, thereby changing their physical, chemical and optical characteristics. In 1857, Michael Faraday analysed the unique properties of metallic nanoparticles and concluded that gold produced unusual colours at small size scales. In 1908, Gudtav Mie made an observation on the optical properties of gold at small size scales as compared to bulk properties (Leon, et al., 2020). The invention of scanning tunnelling microscope (STM) by Gerd Binning and Heinrich Rohrer as well as atomic force microscope (AFM) by Gerd Binnig, Calvin Quate and Christoph Gerber was the first step for researchers to discover the applications in the nanotechnology sector. Both instruments are used to revolutionize imaging and manipulate nano-sized objects. Over the years, nanotechnology has wide applications in distinct areas such as agriculture, electronic, energy, health and cosmetics (Kargozar and Mozafari, 2018).

Nanoparticles are classified as materials with a scale ranging from 1-100 nm (Khan, et al., 2017). Nanoparticles are of profound scientific interest because they span the aperture between bulk materials and atomic or molecular structures. When the bulk materials are in nanoscale, many fascinating features

have been discovered (Thakkar, et al., 2010). The significant feature of nanotechnology is most of the nanoscale materials have large surface area over volume ratio, which makes them very reactive. As a result of large surface area over volume ratio, the surface, interfacial and chemical properties of nanoparticles are ideal for catalyst. This is very important in many applications such as catalysis, electronics, solar energy conversion, water treatment, biomedical and drug delivery (Patra and Baek, 2014; Nasrollahzadeh, et al., 2019).

1.2 Synthesis of Nanoparticles

There are two unique methodologies to synthesise nanoparticles which are top-down approach and bottom-up approach. The top-down synthesis is a destructive approach, in which the suitable bulk materials are decomposed into smaller fine particles and the fine particles are converted into suitable nanoparticles. Various physical, chemical and thermal techniques of top-down synthesis are grinding, sputtering, thermal or laser ablation. On the other hand, the bottom-up synthesis is a building up approach. Nanoparticles are synthesized by gathering or combining atoms to new nuclei then nano-sized particles are grown. The methods include sol gel, spinning, biochemical synthesis and green synthesis (Khan, et al., 2017; Gour and Jain, 2019).

In top-down approach, flawless edges and surfaces are impossible to achieve due to roughness and voids that always happen in nanoparticles. Conversely,

perfect nanoparticles can be produced by bottom-up approach. In addition, other advantages of bottom-up approach include no waste materials generated, better control of nanoparticles' sizes and smaller size of nanoparticles can be obtained (Nadaroğlu, et al., 2017).

Over the years, several physical, chemical, biological and hybrid approaches have been developed for the synthesis of nanoparticles, as shown in Appendix A. However, the synthesis of nanoparticles by traditional physical and chemical techniques involves uses of toxic chemicals as non-biodegradable reducing agents, stabilizing agents or organic solvents, production of hazardous side products, excessive consumption of energy and high cost instrument along with the non-standard condition which may jeopardise the environment and biological systems (Thakkar, et al., 2010; Prabhu and Poulose, 2012; Nadaroğlu, et al., 2017). Therefore, it is crucial to evolve a simple, low cost and ecofriendly approach for the synthesis of useful nanoparticles.

On various aspects, nanoparticles synthesized by green technology outperform those produced with physical and chemical processes. The advantages include avoiding the use of costly chemicals, consuming less energy and producing ecologically benign products and by-products (Patra and Baek, 2014). Biosynthesis of nanoparticles is a bottom-up approach that mostly incorporates oxidation/reduction reactions (Prabhu and Poulose, 2012).

1.3 Zinc Oxide Nanoparticles

Zinc oxide is a n-type semiconductor with a large excitation binding energy of 60 meV and a huge band gap of 3.37 eV. It is a multifunctional material that has high electron mobility, photostability, chemical and thermal stability, strong electrochemical coupling coefficient, wide variety of radiation absorption, and it is non-toxic. These properties make it appealing for prospective usage in laser technology, electronics and optoelectronics (Wang, et al., 2005; Bacaksiz, et al., 2008; Kołodziejczak-Radzimska and Jesionowski, 2014).

Furthermore, zinc oxide nanoparticles are very useful in photocatalysis to degrade numerous organic contaminants in aqueous medium. The surface area of photocatalyst has a significant impact on the photocatalytic activity since photocatalytic activity occurs mostly at the catalyst's surface. Hence, the zinc oxide with nano-size has high potential since it has large surface area to enhance the photocatalytic efficiency (Aminuzzaman, et al., 2019).

1.4 Peppermint Tea Dregs

Tea is a widely consumed and low-cost beverage that is highly valued all across the world. On a daily basis, approximately three billion cups of tea are taken across the world (Hicks, 2009). Tea dregs is one of the waste products in tea industry and the fabrication of tea dregs increases year by year. Majority of

the tea dregs are burnt and disposed as agricultural waste. In recent decades, herbal teas have had an increasing interest both in medicinal and non-medicinal applications (Kapp, et al., 2013).

Peppermint tea (*Mentha piperita*) is one of the most famous single component herbal tea, well-known for its freshening flavour and scent. It is a perennial herb native to Europe that has become naturalised in the northern United States and Canada, as well as being grown in many other countries. Many cosmetic, food and pharmaceutical products use the extracting essential oil from the leaves. Its phenolic constituents comprise of rosmarinic acid and some flavonoids, predominantly eriocitrin, luteolin and hesperidin. Menthone and menthol are the two major volatile components in peppermint (McKay and Blumberg, 2006).

According to Eastern and Western traditions, peppermint is used as a traditional medicine or substitute medical therapy such as indigestion, nausea, vomiting, flatulence, cough, bronchitis and irritable bowel syndrome (Grigoleit and Grigoleit, 2005; Shkurupii, et al., 2006). On top of that, the essential oil or extract of *Mentha piperita* owns radioprotective, insecticidal, fungicidal, antiviral, antimicrobial and antioxidant actions (McKay and Blumberg, 2006; Peixoto, et al., 2009; Rita and Animesh, 2011).

1.5 Problem Statements

Textile industry is one of the most polluting sectors in the universe, consuming large amount of fuels and chemicals. The main environmental harms caused by textile industry are those stemming from the untreated effluents discharge into water bodies (Bhatia and Devraj, 2017). The prominence should be accredited to the vast amount of non-biodegradable organic substances, particularly textile dyes (Orts, et al., 2018).

The production of dye in the world is nearly 800,000 tons per year. In recent years, reducing the quantity of residual dye in textile effluent has become a critical issue. Dyes in the water absorb and reflect sunlight, diminishing the photosynthesis of algae and severely influencing the food chain. Several dyes and their breakdown products are carcinogenic, mutagenic and poisonous. Textile dyes can also trigger allergies such as allergic reactions in eyes, skin, mucous membrane and upper respiratory tract as well as contact dermatitis and respiratory illnesses (Wani, et al., 2019).

Photocatalytic degradation of dyes is a method to remove dyes from wastewater by using photocatalyst. Photocatalysis is a photo-activated chemical reaction that occurs when a substance encounters photons of adequate energy levels and triggers a free radical mechanism (Dobson and Burgess, 2007). Photocatalysis involves the use of a semiconductor and light to accelerate processes. A photocatalyst is a substance that absorbs light and

functions as a catalyst in chemical reactions. Semiconductors can conduct electricity in the presence of light even at ambient temperature, making them suitable photocatalysts (Ameta, et al., 2018).

During the dye degradation activity, large molecules are oxidized into smaller molecules such as carbon dioxide, water and other minerals as by-products. The mechanism of the photocatalytic degradation process is shown in Figure 1.5.1.

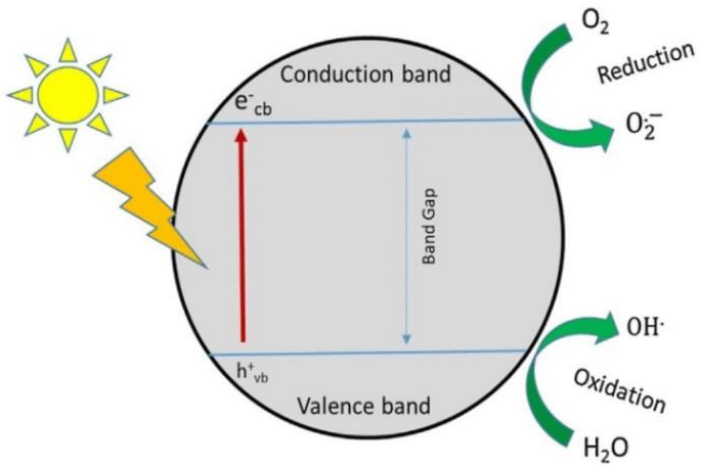

Figure 1.5.1: Schematic diagram of photocatalytic degradation mechanism (Isai and Shrivastava, 2019)

According to Ajmal and his co-workers (2014), there are three main active species available for oxidising the organic contaminants, which include holes (h^+), hydroxyl radicals (OH•) and superoxide radicals ($O•_2^-$). At the initial stage of photocatalysis, electrons of the conduction band (e_{cb}^-) and holes of the valence band (h_{vb}^+) are generated when the suspension is irradiated with

sufficient energy superior to the band gap energy of photocatalyst, as shown in Equation 1.1.

Photocatalyst + hv (UV) → h_{vb}^{+} + e_{cb}^{-} (Eq. 1.1)

Next, for the generation of radicals, the valence band hole will oxidise water or OH^- to generate hydroxyl radicals, shown in Equations 1.2-1.3. On the other hand, the conduction band electron will reduce dissolved molecular oxygen to generate superoxide radicals, shown in Equation 1.4.

$h_{vb}^{+} + H_2O \rightarrow H^+ + OH\bullet$ (Eq. 1.2)

$h_{vb}^{+} + OH^- \rightarrow OH\bullet$ (Eq. 1.3)

$O_2 + e_{cb}^{-} \rightarrow O\bullet_2^-$ (Eq. 1.4)

The superoxide radicals get protonated to form hydroperoxyl radicals (HOO•) and subsequently H_2O_2 which further dissociates into hydroxyl radicals, as shown in Equations 1.5-1.7.

$O\bullet_2^- + H^+ \leftrightarrow HOO\bullet$ (Eq. 1.5)

$2\ HOO\bullet \rightarrow H_2O_2 + O_2$ (Eq. 1.6)

$H_2O_2 \rightarrow 2\ OH\bullet$ (Eq. 1.7)

Lastly, the organic pollutant in the wastewater is oxidised by the highly reactive hydroxyl radicals to form different intermediates which then oxidise to harmless and colourless carbon dioxide and water, as shown in Equation 1.8.

$OH\bullet + dyes \rightarrow CO_2 + H_2O$ (Eq. 1.8)

1.6 Research Objectives

There are five objectives in this project which include:

i) To synthesise zinc oxide nanoparticles via a green synthetic route using peppermint tea (*Mentha piperita*) dregs extract.

ii) To determine the bioactive compounds present in peppermint tea (*Mentha piperita*) dregs extract by carrying out qualitative phytochemical screening.

iii) To study the effects of mass of zinc nitrate hexahydrate and calcination temperature on the synthesis of zinc oxide nanoparticles.

iv) To characterise the zinc oxide nanoparticles by Fourier transform infrared spectroscopy (FTIR), ultraviolet-visible spectroscopy (UV-Vis), X-ray diffraction (XRD), field emission scanning electron microscopy (FESEM), energy dispersive X-ray analysis (EDX) and particle size analysis (PSA).

v) To evaluate the photocatalytic performance of zinc oxide nanoparticles synthesised in the degradation of crystal violet dye under solar irradiation.

1.7 Scope of Research

In this project, there are a few research scopes that are required to be taken into account.

i) To possess a green synthesis method, agricultural waste is used as the raw materials and deionised water is used as the solvent in the preparation of peppermint tea dregs extract and also the synthesis of zinc oxide nanoparticles.

ii) Qualitative phytochemical screening is conducted to detect the bioactive compounds present in the peppermint tea dregs extract such as Dragendorff's test and Wagner's test (test for alkaloids), alkaline reagent test and lead acetate test (test for flavonoids), foam test (test for saponins), ferric chloride test (test for tannins), Keller Killiani test (test for glycosides) and xanthoproteic test (test for proteins).

iii) Mass of zinc nitrate hexahydrate and calcination temperature are two parameters in the synthesis of zinc oxide nanoparticles.

iv) The characterisation of zinc oxide nanoparticles synthesized is performed to determine its morphology, shape and size via various analytical techniques such as Fourier transform infrared spectroscopy (FTIR), ultraviolet-visible spectroscopy (UV-Vis), X-ray diffraction (XRD), field emission scanning

electron microscopy (FESEM), energy dispersive X-ray analysis (EDX) and particle size analysis (PSA).

v) The photocatalytic efficiency of zinc oxide nanoparticles synthesised is evaluated by the degradation of crystal violet dye with the exposure of sunlight.

1.8 Significance of Research

The primary focus in this project is to use agricultural waste to synthesise zinc oxide nanoparticles and subsequently reduce the disposal of agricultural waste. Green synthesis is used to convert useless agricultural waste into useful zinc oxide nanoparticles to possess a cost-effective, harmless, simple, safe, non-toxic and environmentally friendly route. The presence of bioactive compounds in the peppermint tea dregs extract is determined to investigate the ability of those compounds serving as reducing agent or capping agent in the synthesis of zinc oxide nanoparticles. The importance of zinc oxide nanoparticles on photodegradation of dye is discussed to find its potential applications in industrial wastewater treatment with the main purpose of diminishing water pollution.

CHAPTER 2

LITERATURE REVIEW

2.1 Green Synthesis

Efforts are being undertaken all over the world to develop environmentally friendly technologies that use green nanotechnology and biotechnological techniques to generate ecologically benign, harmless products (Joerger, et al., 2000; Chauhan, et al., 2012). Nanoparticles synthesised using biological means or green technology offer a variety of properties including increased stability and appropriate dimensions since they are synthesised using a one-step approach (Patra and Baek, 2014).

Green synthesis is more productive to synthesize nanoparticles with advantages of safe, cost-effective, low energy, eco-friendly, simple and reproducible technique (Nadaroğlu, et al., 2017). Green synthesis is the synthesis of nanoparticles using biological methods involving plants or microorganisms. Microbial enzymes and plant phytochemicals such as proteins, alkaloids, phenolic compounds with reducing properties primarily operate on the compounds to produce the required nanoparticles (Prabhu and Poulose, 2012). Figure 2.1.1 depicts how biological methods produce nanoparticles.

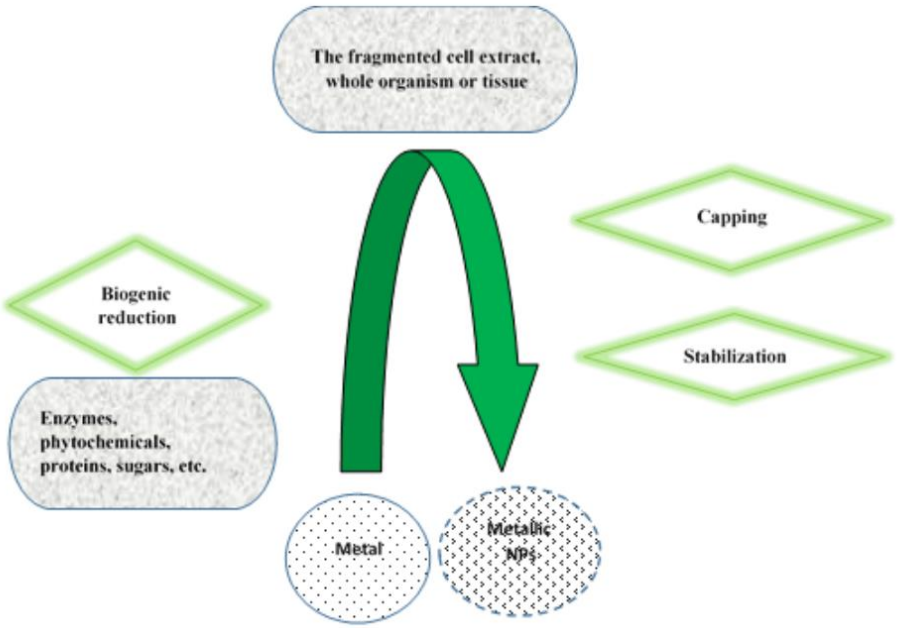

Figure 2.1.1: Synthesis process of nanoparticles by biological methods (Hussain, et al., 2016)

However, using microorganisms to synthesise nanoparticles requires more steps in sustaining cell culture and extra purification procedures. Therefore, green synthesis using plant extracts is relatively easier and simpler technique. Green nanoparticle synthesis utilising plant extracts has recently gained popularity due to various benefits such as biocompatibility, biosafety, cost-effectiveness, non-toxicity and synthesis in ambient atmosphere (Aminuzzaman, et al., 2019).

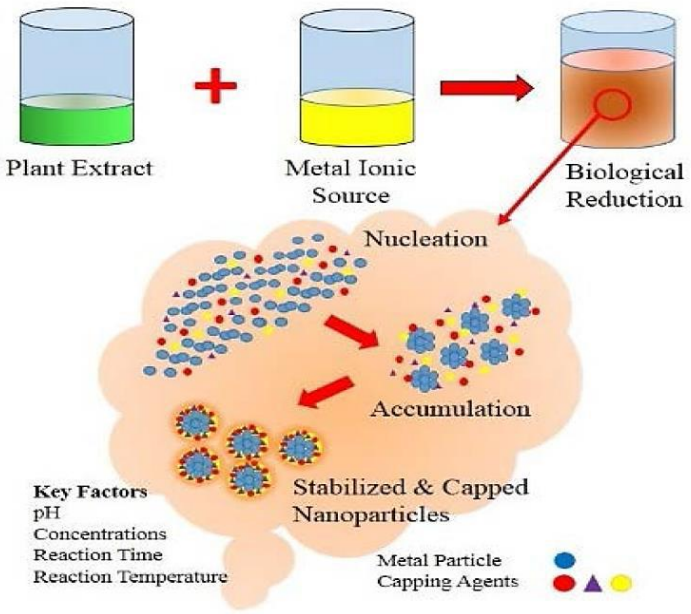

Figure 2.1.2: Schematic diagram for the synthesis of nanoparticles by biological method using plant extract (Shah, et al., 2015)

2.2 Green Synthesis Using *Corymbia Citriodora* Leaf Extract and Their Photocatalytic Activity

In this work by Zheng and his co-workers (2015), synthesis of zinc oxide nanoparticles by biological method was carried out in a green and effortless manner using *Corymbia citriodora* leaf extract as stabilizing agent and reducing agent with zinc nitrate as salt precursor. *Corymbia citriodora* is a gigantic tree native to northern Australia's temperate and tropic regions. Citronellal is the main chemical component of *C. citriodora*, a plant with reducing properties.

The SEM image implies that the ZnO NPs exhibit excellent dispersibility and the TEM image reveals that the ZnO NPs are polyhedron-shaped with size

ranging from 20-120 nm as analysed by particle size analyser. Figure 2.2.1(d) illustrates the EDX profile of sample in which only Zn and O are present, implying that the ZnO NPs produced are of high purity.

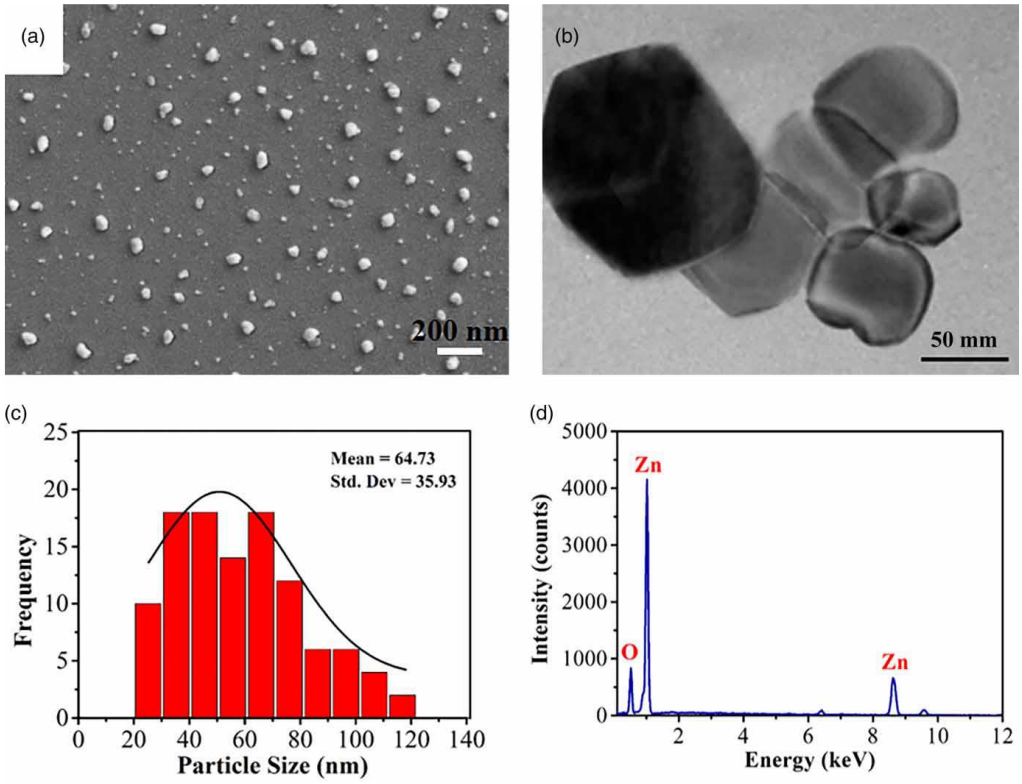

Figure 2.2.1: (a) SEM image, (b) TEM image, (c) Particle size distribution graph and (d) EDX profile of ZnO NPs

Figure 2.2.2 displays the FTIR spectrum of *C. citriodora* leaf extract. The intense absorption peaks at 3300 and 1620 cm^{-1} can be attributed to O-H stretching vibration and N-H bending vibration. Subsequently, there are weaker bands at 2955, 777 and 633 cm^{-1} which can be attributed to -C-H (alkanes), -C-H (aromatics) and -C=C-H (alkynes) stretches. The C=C bending and C-C stretching of aromatic rings show absorption peaks at 1520 and 1431

cm^{-1} respectively. Lastly, the peak at 1053 cm^{-1} is assigned to the C-N stretching vibration in aliphatic amine.

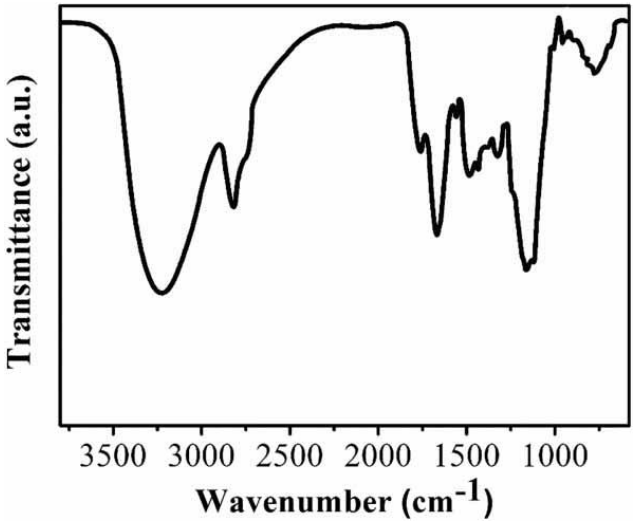

Figure 2.2.2: FTIR spectrum of *C. citriodora* leaf extract

Figure 2.2.3(a) shows the XRD spectrum of synthesized ZnO NPs. The peaks at 32.1°, 34.6°, 36.1°, 47.7°, 56.4°, 63.1° and 68.1° can be discovered to hexagonal wurtzite phase of ZnO. No additional peaks are seen, signifying that the synthesized ZnO NPs are of great purity. From the XRD peaks and by using Scherrer's equation, the mean crystallite size is determined to be 21 nm. The UV-Vis spectrum of the biosynthesized ZnO NPs is shown in Figure 2.2.3(b). The spectrum gives an absorption peak at 386 nm and the band gap energy of ZnO NPs can be found as 3.07 eV.

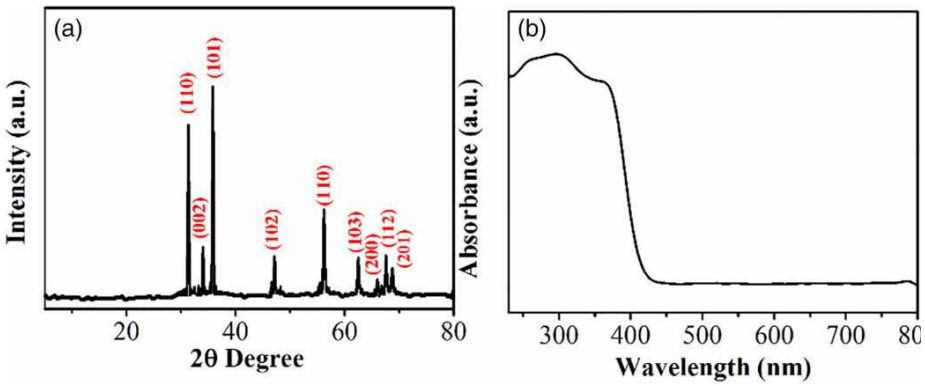

Figure 2.2.3: (a) XRD spectrum and (b) UV-Vis spectrum of biosynthesized ZnO NPs

The degradation of methylene blue under sun irradiation was used to assess the photocatalytic performance of the ZnO NPs. The ZnO NPs synthesised have been found to exhibit outstanding photocatalytic activity. Biosynthesized ZnO and hydrothermally synthesized ZnO degraded 83.45 % and 59.47 % of methylene blue respectively after 90 minutes of irradiation. The excellent photocatalytic performance of biosynthesised ZnO may be owing to its smaller size in contrast with hydrothermal synthesised ZnO NPs, which may contribute larger surface area to absorb and degrade dye molecules.

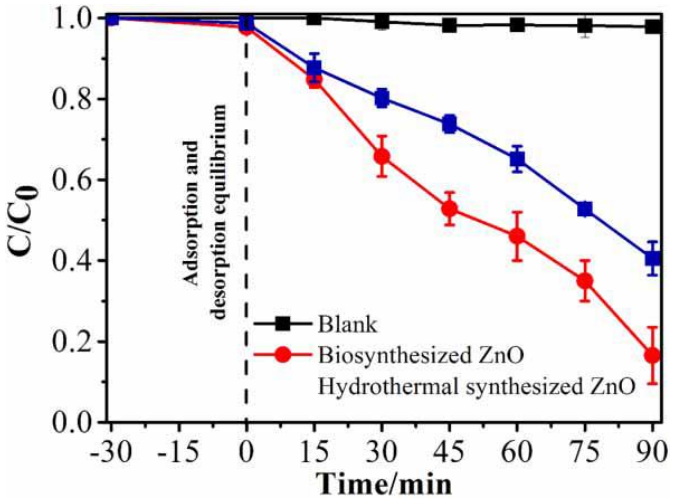

Figure 2.2.4: Photodegradation of MB dye under solar irradiation with the presence and absence of different ZnO NPs

2.3 Green Synthesis Using Dragon Fruit (*Hylocereus Polyrhizus*) Peel Biowaste and Their Photocatalytic Activity

According to this work reported by Aminuzzaman and his co-workers (2019), dragon fruit peel extract was used in the synthesis of zinc oxide nanoparticles as reducing and stabilizing agent as well as zinc nitrate as salt precursor at 450 °C calcination temperature. Dragon fruit is a tropical fruit that is from the cactus family *Cactaceae*.

The findings of the characterisation reveal that the synthesized ZnO NPs are spherical and have a mean size of 56 nm. The ZnO NPs have hexagonal wurtzite phase and are well-crystalline. As shown in Figure 2.3.1, the distinct peaks of diffraction at 2θ positions with the values of 31.88°, 34.42°, 36.38°, 47.78°, 56.78°, 63.04°, 66.64°, 68.14°, 69.25°, 73.59° and 72.38° are

corresponding to the ZnO lattice planes of (100), (002), (101), (102), (110), (103), (200), (112), (201), (004), and (202) respectively, which indicate hexagonal wurtzite phase. Using Debye-Scherrer's equation, the crystallize size of the nanoparticles is determined to be 51 nm.

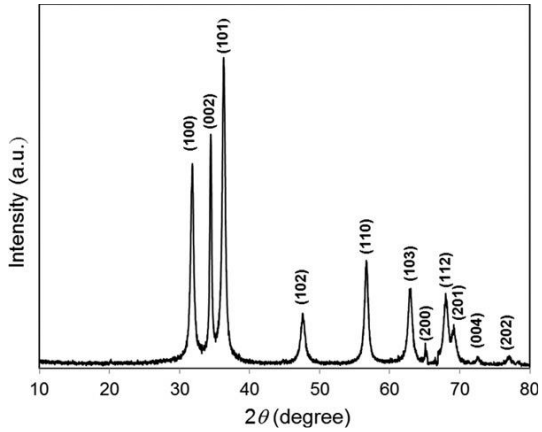

Figure 2.3.1: XRD spectrum of ZnO NPs synthesised using dragon fruit peel extract

The EDX profile in Figure 2.3.2 confirmed the existence of Zn and O with no additional elemental contamination.

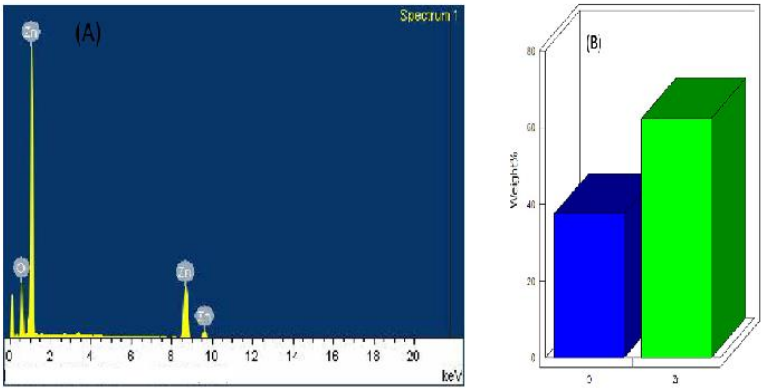

Figure 2.3.2: (A) EDX profile of ZnO NPs synthesised and (B) Weight percent of each element

TEM was used to study the morphology and size of the ZnO NPs, as shown in Figure 2.3.3. It has shown that the synthesized ZnO NPs are predominantly spherical, varying in size from 5-100 nm.

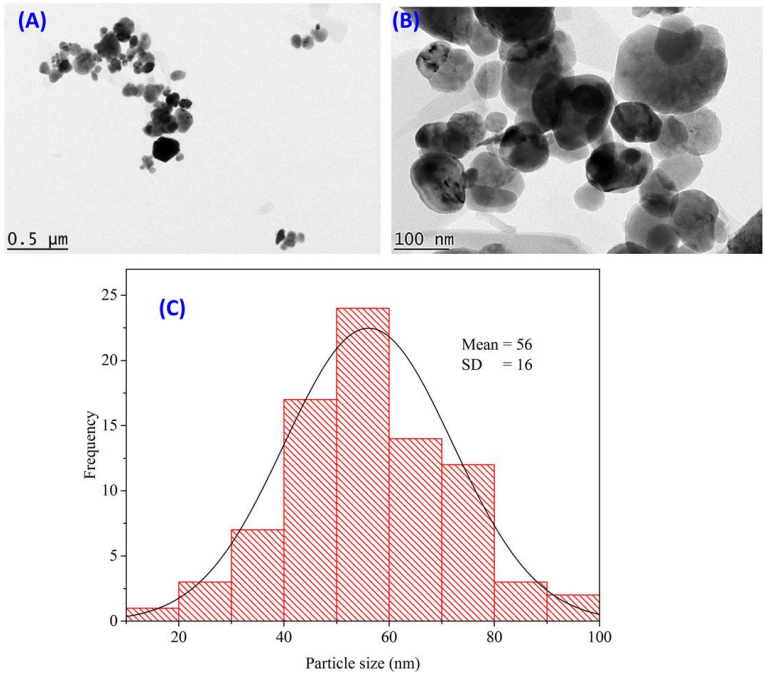

Figure 2.3.3: TEM images at different magnifications and particle size distribution of the synthesised ZnO NPs

Figure 2.3.4 demonstrates the FESEM images of ZnO NPs, showing that particles are spherical, consistent with TEM images. The ZnO NPs are in high density and homogeneous dispersion.

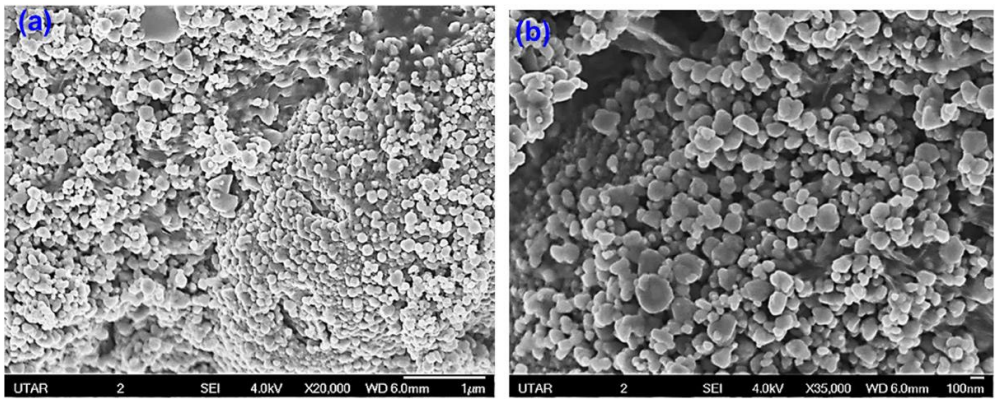

Figure 2.3.4: FESEM images of ZnO NPs synthesized at different magnifications

An absorption peak at 369 nm is observed in the UV-Vis spectrum owing to the electron transitions from valence band to conduction band and the band gap energy is determined as 3.36 eV. The synthesised ZnO NPs are of high purity and with excellent optical properties since there is no extra peak observed in the spectrum.

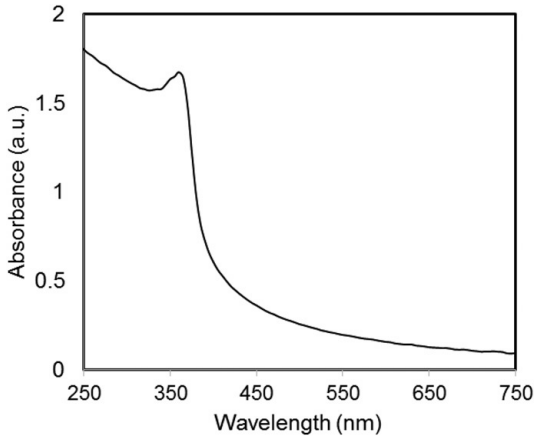

Figure 2.3.5: UV-Vis spectrum of ZnO NPs synthesised

Figure 2.3.6 displays the FTIR spectra of dragon fruit peel extract and zinc oxide nanoparticles synthesised. The dragon fruit peel extract shows peaks at 3432 cm^{-1} (O-H stretching), 2972 cm^{-1} (C-H stretching), 1637 cm^{-1} (C=O stretching), 1399 cm^{-1} (C-C stretching), 1248 cm^{-1} (C-O stretching) and 1054 cm^{-1} (C-O-C stretching). The Zn-O stretching vibration is responsible for the peak observed at 460 cm^{-1}.

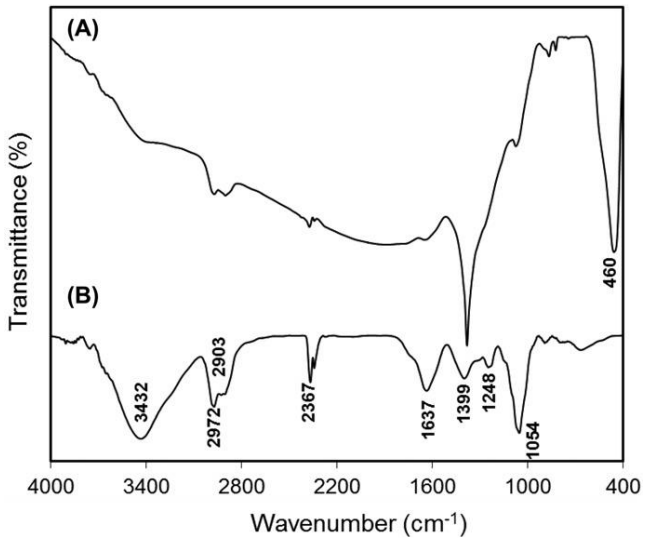

Figure 2.3.6: FTIR spectra of (A) synthesized ZnO NPs and (B) dragon fruit peel extract

Next, the photocatalytic performance of ZnO NPs has been examined by the degradation of MB under direct solar illumination in open environment as follows: (i) without photocatalyst under sunlight (ii) with photocatalyst in dark and (iii) with photocatalyst under sunlight.

When the ZnO NPs totally deteriorated the methylene blue, the solution turned from dark blue to colourless. This proves that the ZnO NPs possess outstanding photocatalytic efficiency and can degrade methylene blue dye completely. The highest absorption peak of MB rapidly decreased with increasing time of exposure to sunlight, meaning that the structure has changed caused by the destruction of chromophores in the dye molecules. With increasing exposure time, the highest absorption wavelength likewise shifted from 665 to 655 nm, implying a N-demethylation process during

photodegradation. The pure nano-sized green-synthesised ZnO NPs resulted in exceptional photocatalytic activity.

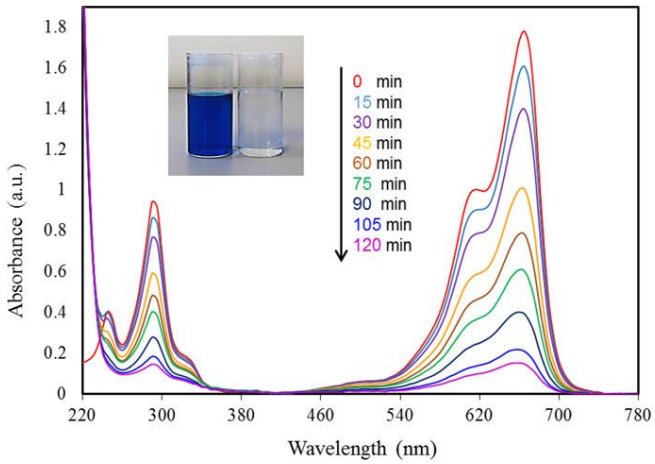

Figure 2.3.7: UV-Vis spectrum of MB dye under sun irradiation with reaction time

In contrast, the results reveal that there was no substantial photodegradation either under sunlight without ZnO NPs or vice versa, proving the synergistic impact of synthesized ZnO NPs and sun irradiation on the methylene blue dye photodegradation.

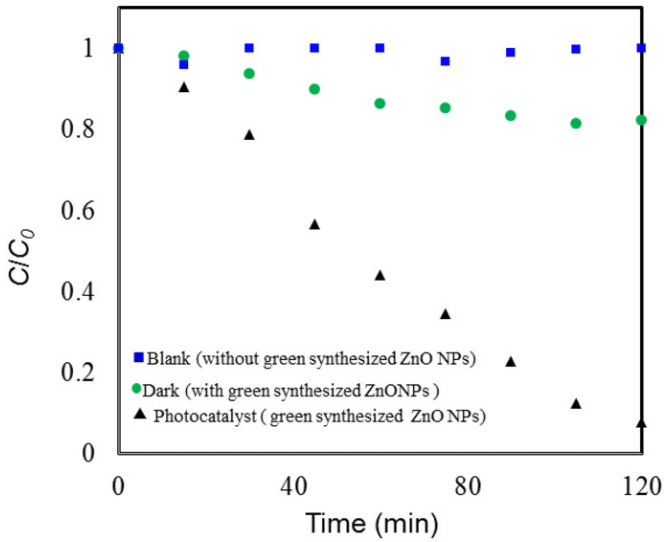

Figure 2.3.8: MB dye degradation efficiency under various conditions

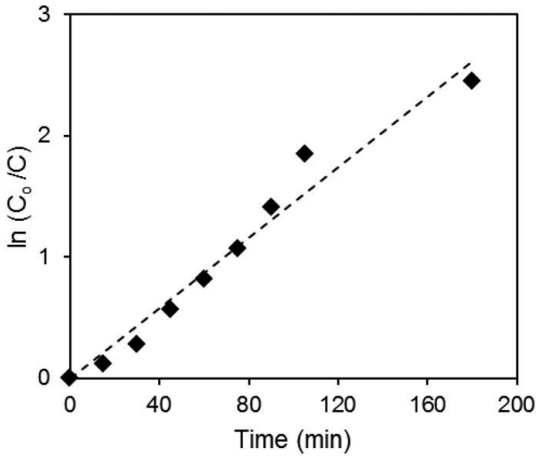

Figure 2.3.9: Plot of $\ln(C_0/C)$ for the MB dye photodegradation versus exposure time in the presence of ZnO NPs as photocatalyst

2.4 Green Synthesis Using Rice Bran Extract and Their Photocatalytic Activity

Fatimah (2018) reported that biosynthesis of ZnO NPs using rice bran was performed. The synthesis was carried out by refluxing the rice bran extract

dissolved in ethanol with zinc acetate dihydrate as precursor. According to the findings, the ZnO NPs synthesised have a 17.16 nm average particle size and a 3.18 eV band gap energy.

The phase of ZnO NPs was confirmed by X-ray diffraction, as shown in Figure 2.4.1. The XRD peaks are observed at (100), (002), (101), (012), (110), (013), (220), (112), and (201) planes as the evidence of ZnO wurtzite. The high intensity diffraction peaks suggest that the zinc oxide is well-crystalline. Wulfingite $Zn(OH)_2$ are detected in a few additional peaks, which suggests that the ZnO has not been completely transformed in the synthesis. The mean particle size of the ZnO NPs is found to be 17.60 nm.

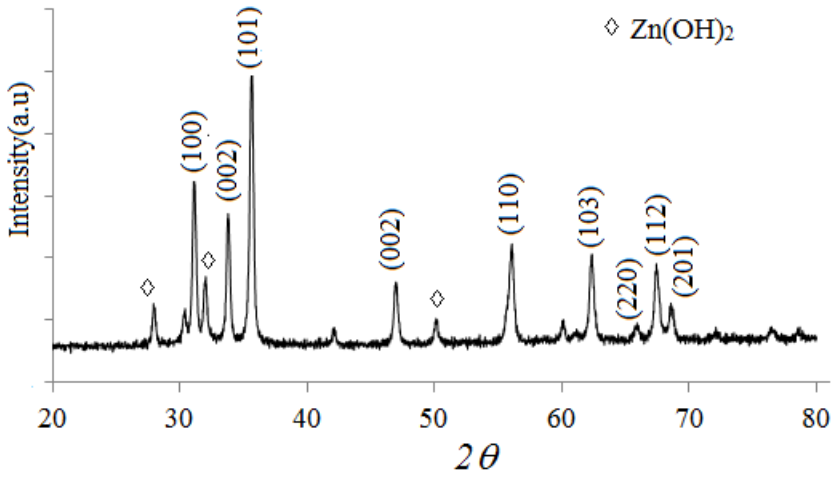

Figure 2.4.1: XRD spectrum of ZnO NPs synthesized

Figure 2.4.2 shows the SEM images of the synthesized ZnO NPs at 5000x and 10,000x magnifications. The ZnO NPs are in amorphous aggregates and needle-like form. The distinction in shape may be associated with different

thermal decomposition effect during calcination. Previous research has discovered that thermal decomposition at 430 ℃ can result in the development of needle-like ZnO NPs from rhombic $Zn(OH)_2$.

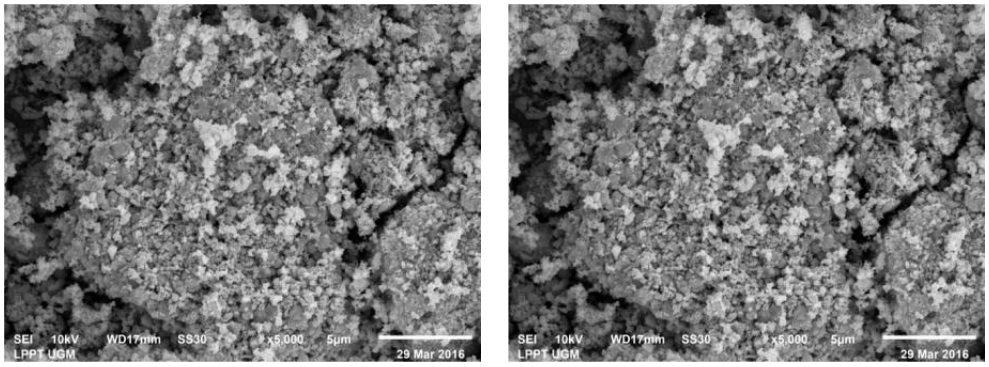

Figure 2.4.2: SEM images of ZnO NPs at 5000x and 10,000x magnifications

The UV-Vis spectrum of the nanoparticles presented in Figure 2.4.3 implies that the λ of 389.9 nm corresponds to the band gap energy of 3.18 eV. This indicates that the nanoparticles have the capacity to absorb photons due to the band gap potential for photocatalytic application.

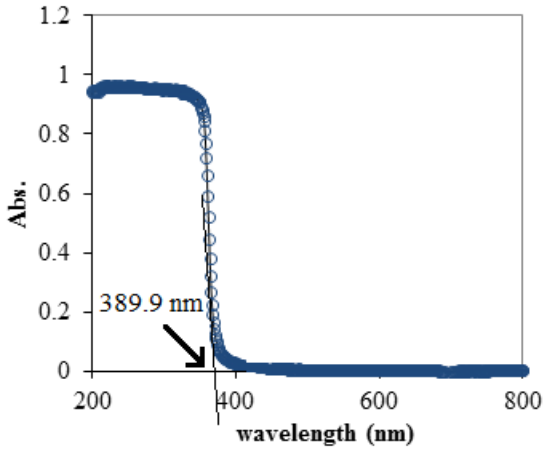

Figure 2.4.3: UV-Vis spectrum of the ZnO NPs

The photocatalytic performance of ZnO NPs synthesised was assessed by the photodegradation of bromo phenol blue (BPB). With increasing time, there was a disappearance of peak at approximately 597 nm, a reduction in intensity and a peak shift at 310 nm. Generally, the photocatalytic activity of ZnO NPs is nearly correlated to the band gap energy of 3.18 eV which is responsible for the mechanism of photocatalysis.

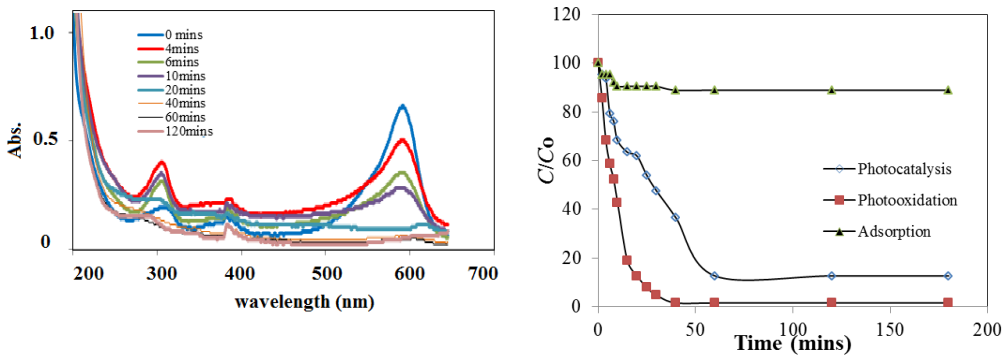

Figure 2.4.4: (a) UV-Vis spectrum of BPB (b) Kinetics of BPB degradation under various conditions

2.5 Concluding Remarks

Based on the previous studies, zinc nitrate hexahydrate was chosen as the salt precursor for this study as it is the best as compared to other types of zinc salt such as zinc acetate dihydrate. Previous studies have also reported that mass of salt precursor chosen can affect the size of nanoparticles synthesised as well as different calcination temperatures can change the morphology of the zinc oxide nanoparticles synthesised. Therefore, mass of zinc nitrate hexahydrate and calcination temperature were selected as the two parameters in this study.

CHAPTER 3

METHODOLOGY

3.1 Materials

In this project, the agricultural waste selected to be used as the feedstocks for the synthesis of zinc oxide nanoparticles was peppermint tea (*Mentha piperita*) dregs. The peppermint tea used was purchased from Lotus's Malaysia in Kampar, Perak. The key chemical which was the zinc nitrate hexahydrate, $Zn(NO_3)_2.6H_2O$ was provided by HiMedia Laboratories and its molecular weight is 297.49 g/mol. Throughout this project, deionised water was used as the solvent for the synthesis as well as the cleaning solvent to rinse the glassware. In addition, the ethanol used to prepare the test solutions for phytochemical screening and the crystal violet dye used in the photocatalysis were supplied by Systerm Chemicals and Bio Basic Canada respectively.

For the qualitative phytochemical screening of peppermint tea dregs extract, the chemical reagents used included Dragendorff's reagent, Wagner's reagent, 1 M sodium hydroxide (NaOH), dilute acetic acid (CH_3COOH), 10 % lead acetate ($Pb(CH_3COO)_2$), 2 M hydrochloric acid (HCl), 5 % ferric(II) chloride ($FeCl_2$), ferric(III) chloride ($FeCl_3$), glacial acetic acid (CH_3COOH), concentrated sulphuric acid (H_2SO_4) and concentrated nitric acid (HNO_3).

3.2 Equipment

The equipment employed in this project are listed in Table 3.2.1 along with their functions.

Table 3.2.1: List of equipment and their functions

No.	Equipment	Function
1	Oven	To remove moisture from the peppermint tea dregs.
2	Grinder	To grind the peppermint tea dregs into powder form.
3	Desiccator	To store the peppermint tea dregs powder and zinc oxide nanoparticles for further use.
4	Electronic weighing balance	To weigh the peppermint tea dregs, zinc nitrate hexahydrate, zinc oxide nanoparticles and crystal violet dye.
5	Hot plate with magnetic stirrer	To heat the extract with constant stirring and synthesise zinc oxide nanoparticles as well as constantly stir the dye solution during photodegradation process.
6	Thermometer	To monitor the temperature when heating the extract.
7	Furnace	To heat and calcinate the brown paste obtained at a very high temperature.

Table 3.2.1 continued: List of equipment and their functions

8	Mortar and pestle	To grind the zinc oxide nanoparticles synthesised into finer particles.
9	Sonicator	To disperse the zinc oxide nanoparticles in deionised water.
10	Freeze dryer	To remove water or other solvent from the peppermint tea dregs extract.
11	Centrifuge	To separate zinc oxide nanoparticles from degraded dye solution.

3.3 Instruments

Table 3.3.1 lists the instruments utilised for the characterisation of zinc oxide nanoparticles as well as their functions.

Table 3.3.1: List of instruments and their functions

No.	Instrument	Model	Function
1	Fourier transform infrared spectrometer (FTIR)	PerkinElmer Spectrum RX 1	To identify the functional groups present in the peppermint tea dregs extract and zinc oxide nanoparticles.

Table 3.3.1 continued: List of instruments and their functions

2	UV-visible spectrophotometer (UV-Vis)	Thermo Fisher Scientific Genesys 50	To determine the absorption value of zinc oxide nanoparticles and monitor the photodegradation process.
3	X-ray diffraction (XRD)	Shimadzu XRD 6000	To determine the crystallinity of zinc oxide nanoparticles.
4	Field emission scanning electron microscope (FESEM)	Jeol JSM-6701F	To identify the morphology and determine the particle size range of zinc oxide nanoparticles.
5	Energy dispersive X-ray spectrometer (EDX)	Oxford Instruments X-Max 50mm^2	To determine the elemental composition of zinc oxide nanoparticles.
6	Particle size analyser (PSA)	Malvern Panalytical Mastersizer Hydro 2000MU	To determine the particle size range of zinc oxide nanoparticles.

3.4 Flow Chart of Overall Process

Figure 3.4.1 presents the flow chart of overall process in this research project. The peppermint tea dregs extract was prepared and proceeded to qualitative phytochemical screening to detect the presence of bioactive compounds. After

that, the peppermint tea dregs extract was used to synthesise zinc oxide nanoparticles and the zinc oxide nanoparticles synthesised was characterised via various analytical methods. Lastly, the best zinc oxide nanoparticles synthesised was selected and evaluated for its photocatalytic performance.

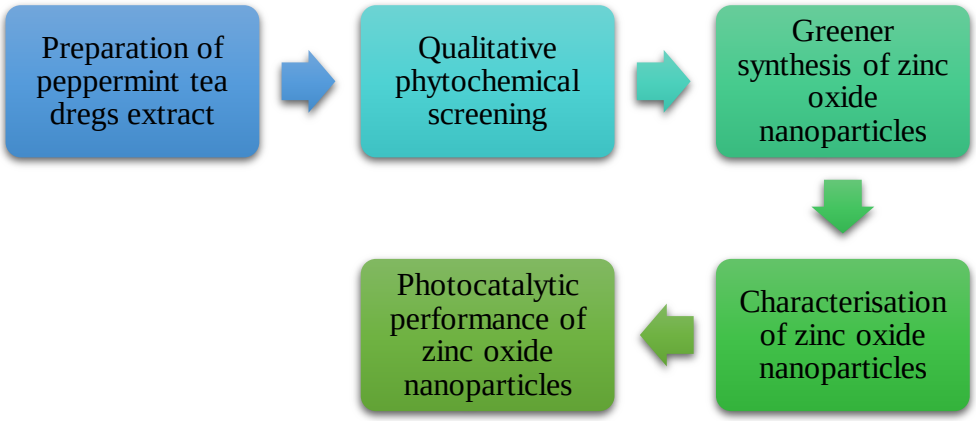

Figure 3.4.1: Flow chart of overall process

3.5 Preparation of Peppermint Tea Dregs Extract

Peppermint tea dregs was cleaned with deionised water to remove impurities and particulate matter. Then, the tea dregs was dried in the oven at 80 °C for 18 hours to get rid of moisture. The dried tea dregs was ground into fine powder using grinder to increase the surface area as to maximise the extraction. The tea dregs fine powder was stored in a desiccator for further operation.

After that, 5 g of tea dregs fine powder were weighed and added with 200 mL of deionised water. The mixture was heated at 70-80 °C for 20 minutes with

constant stirring. The extraction temperature was optimum for preserving the maximum bioactive compounds as the bioactive compounds might be broken down at higher temperatures. Then, the tea dregs extract was cooled and filtered twice to remove large agglomerates and insoluble fractions. The filtrate was kept at 4 °C to prevent microbial contamination.

3.6 Qualitative Phytochemical Screening

Qualitative phytochemical screening was conducted to detect the presence of bioactive compounds such as alkaloids, flavonoids, saponins, tannins, glycosides and proteins in the peppermint tea dregs extract. The test solutions for phytochemical screening were prepared by dissolving the peppermint tea dregs extract in ethanol in a ratio of 1:10 (Tugiyanti, et al., 2019).

3.6.1 Test for Alkaloids

3.6.1.1 Dragendorff's Test

The test solution was reacted with Dragendorff's reagent to detect alkaloids. The formation of orange precipitate indicated the presence of alkaloids (Tugiyanti, et al., 2019).

3.6.1.2 Wagner's Test

Two to three drops of Wagner's reagent were added into 1 mL of crude extract. The presence of reddish-brown precipitate revealed the presence of alkaloids in the crude extract (Banu and Cathrine, 2015).

3.6.2 Test for Flavonoids

3.6.2.1 Alkaline Reagent Test

Two to three drops of 1 M sodium hydroxide were added into 1 mL of crude extract. Once the test solution turned yellow, a few drops of dilute acetic acid were added. The decolourisation of test solution indicated the presence of flavonoids in the tea dregs extract (Hossain, et al., 2013).

3.6.2.2 Lead Acetate Test

A little amount of 10 % lead acetate was added into the crude extract. The appearance of precipitate implied the presence of flavonoids (Banu and Cathrine, 2015).

3.6.3 Test for Saponins

Foam test was performed. A small amount of crude extract was mixed with 2 mL of deionised water. The saponins portion was detected by the formation of foam after shaking. The formation of foam with a height of 1-10 cm that was stable for over 10 minutes and was not lost upon the introduction of one drop of 2 M hydrochloric acid proved the presence of saponins (Tugiyanti, et al., 2019).

3.6.4 Test for Tannins

Ferric chloride test was carried out. Two to three drops of 5 % ferric(II) chloride were added into 2 mL of crude extract. The colour change to blue green with the formation of precipitate confirmed the presence of tannins (Usman, et al., 2009).

3.6.5 Test for Glycosides

Keller Killiani test was performed. Two to three drops of ferric(III) chloride, 2 mL of glacial acetic acid and 1 mL of concentrated sulphuric acid were added into 2 mL of crude extract. The appearance of a brown ring at the intersection of the two liquid layers and a green ring at the acetic acid layer confirmed the presence of glycosides (Sheel, et al., 2014).

3.6.6 Test for Proteins

Xanthoproteic test was carried out. Two to three drops of concentrated nitric acid were added into 1 mL of crude extract. The colour change to yellow revealed the presence of proteins in the crude extract (Kamineni, et al., 2016).

3.7 Green Synthesis of Zinc Oxide Nanoparticles

The aqueous extract of peppermint tea dregs was used as an eco-friendly reducing agent and stabilising agent to synthesise zinc oxide nanoparticles (ZnO NPs). In this research project, zinc oxide nanoparticles was synthesised by a simple approach involving the reaction between zinc nitrate hexahydrate and the extract from peppermint tea dregs.

The synthesis process was begun by boiling 50 mL of peppermint tea dregs extract at 70-80 °C with constant stirring. Then, 5 g of zinc nitrate hexahydrate were added into the extract with continuous boiling and stirring until brown paste was obtained. The brown paste was relocated into a crucible and was proceeded for calcination at 450 °C for 2 hours in the furnace. The formation of yellowish-white powder confirmed the formation of zinc oxide nanoparticles. The synthesised ZnO NPs was ground into finer particles using mortar and pestle. Lastly, the synthesised ZnO NPs was weighed and stored in desiccator for further characterisation.

The procedures were repeated by using different mass of zinc nitrate hexahydrate which were 10 g, 15 g and 20 g. The mass of zinc nitrate hexahydrate that produced the best zinc oxide nanoparticles was used for the determination of the most suitable calcination temperature among 450 °C, 550 °C, 650 °C and 750 °C.

3.8 Yield of Synthesised Zinc Oxide Nanoparticles

The effects of mass of zinc nitrate hexahydrate and calcination temperature in the synthesis of zinc oxide nanoparticles were studied. The mass of zinc oxide nanoparticles was measured using an electronic weighing balance. The percent yield of the synthesised zinc oxide nanoparticles was calculated using Equation 3.1.

$$Percent\ yield\ of\ ZnO\ NPs = \frac{Mass\ of\ ZnO\ NPs}{Mass\ of\ Zn(NO_3)_2.6H_2O} \times 100\ \%\ \text{(Eq. 3.1)}$$

3.9 Characterisation of Zinc Oxide Nanoparticles

The characterisation of zinc oxide nanoparticles synthesized was conducted to determine its morphology, shape and size via various analytical techniques such as Fourier transform infrared spectroscopy (FTIR), ultraviolet-visible spectroscopy (UV-Vis), X-ray diffraction (XRD), field emission scanning electron microscopy (FESEM), energy dispersive X-ray analysis (EDX) and particle size analysis (PSA).

3.9.1 Fourier Transform Infrared Spectroscopy (FTIR)

The zinc oxide nanoparticles synthesised was ground with potassium bromide (KBr) salt to form KBr pellet which was flat and circular in shape. The pellet was then inserted into the sample slot of PerkinElmer Spectrum RX 1 Fourier transform infrared spectrometer. The infrared spectrum of zinc oxide nanoparticles was recorded from 4000-400 cm^{-1} with 32 scans and 4 cm^{-1} resolution. The peppermint tea dregs extract was also freeze dried into solid for FTIR analysis to determine the functional groups present.

3.9.2 Ultraviolet-Visible Spectroscopy (UV-Vis)

Before subjecting to the Thermo Fisher Scientific Genesys 50 UV-visible spectrophotometer, 5 mg of ZnO NPs were dispersed in 10 mL of deionised water and the dispersion was aided with 15 minutes of sonication. A quartz cuvette was used, and deionised water acted as the blank solution in this analysis. After eliminating the background absorbance, the zinc oxide nanoparticles solution was scanned in the range of 200-800 nm to determine the absorption value of zinc oxide nanoparticles synthesised.

From the maximum wavelength obtained for the zinc oxide nanoparticles, the band gap energy of ZnO NPs could be calculated using Equation 3.2 (Miah, 2021). The band gap energy could be exploited to further confirm that the yellowish-white powder formed was indeed zinc oxide nanoparticles.

$$\text{Band gap energy (E)} = \frac{hc}{\lambda} \text{ (Eq. 3.2)}$$

where h = Planck's constant (6.626×10^{-34} Js), c = speed of light (3.0×10^{8} ms^{-1}), λ = maximum absorption wavelength (nm)

With the conversion factor, the calculated band gap energy was then converted to electron volt (eV) to define the amount of kinetic energy gained by an electron when accelerated in an electric field created by a one-volt potential difference (Bronzino, 2005).

$$1 \text{ eV} = 1.602 \times 10^{-19} \text{ J}$$

3.9.3 X-Ray Diffraction (XRD)

X-ray diffraction was utilised to determine the crystallinity of zinc oxide nanoparticles and affirm the highest FWHM peaks by using Shimadzu XRD 6000 with Cu Kα radiation (1.540600 Å). The zinc oxide nanoparticles was placed on a sample holder and scanned at 40kV/30mA. The scan speed and angular range of the instrument were $2°min^{-1}$ and $10° < 2\theta < 80°$ respectively.

Based on the XRD spectrum, the crystallite size of well-crystalline ZnO NPs could be calculated using Debye-Scherrer equation (Gibson and Holzwarth, 2011).

$$D = \frac{k\lambda}{\beta cos\theta} \text{ (Eq. 3.3)}$$

$$\beta = \frac{FWHM\ in\ 2\theta \times \pi}{180°}$$ (Eq. 3.4)

where D = mean crystallite size (nm), k = Scherrer's constant (usually 0.9), λ = wavelength of X-ray source, Cu Kα radiation (1.540600 Å), β = full width at half maximum (FWHM) of the diffraction peak in radian, θ = Bragg's diffraction angle

3.9.4 Field Emission Scanning Electron Microscopy (FESEM)

The particle size and shape as well as morphology of zinc oxide nanoparticles were determined by Jeol JSM-6701F field emission scanning electron microscope. The ZnO NPs was scanned from lower resolution to higher resolution and from 1,000x to 60,000x of magnification. The results were presented in the form of images.

3.9.5 Energy Dispersive X-Ray Analysis (EDX)

Oxford Instruments X-Max 50mm^2 energy dispersive X-ray spectrometer was used to identify the composition of elements in zinc oxide nanoparticles synthesised.

3.9.6 Particle Size Analysis (PSA)

The particle size range of zinc oxide nanoparticles was measured by Malvern Panalytical Mastersizer Hydro 2000MU particle size analyser. The zinc oxide

nanoparticles was distributed in 50 mL of distilled water. The size range was set to between 0.02 μm and 2000 μm while the particle refractive index and dispersant refractive index were 2.003 and 1.330 respectively. In a 1 L beaker, about 800 mL of distilled water were added, and the beaker was placed under the stirrer of the particle size analyser. The instrument automatically removed the background noise when water was displaced. Once the instrument was stabilised, zinc oxide nanoparticles solution was added slowly into the beaker until the intensity had reached 15 %.

3.10 Photocatalytic Performance of Zinc Oxide Nanoparticles

The photocatalytic performance of zinc oxide nanoparticles was evaluated by the degradation of crystal violet dye solution with exposure to sunlight. In 500 mL of deionised water, 5 mg of crystal violet powder were dissolved to obtain 10 ppm crystal violet dye solution. Four beakers with 50 mL of crystal violet dye solution were prepared and 50 mg of ZnO NPs were added into two of the beakers. Prior to illumination, all the four mixtures were stirred constantly in dark for 30 minutes to obtain equilibrium of adsorption and desorption between dye molecules and ZnO NPs photocatalyst. After 30 minutes, the mixtures were conditioned according to Table 3.10.1.

Table 3.10.1: Variable conditions for the degradation of CV dye

Beaker	ZnO NPs photocatalyst		Condition	
	With	Without	In the dark	Under sunlight
A		✓	✓	
B	✓		✓	
C		✓		✓
D	✓			✓

The mixtures subjected to sunlight were placed at the same spot and at the same time for solar irradiation in order to avoid data bias since the degradability of crystal violet dye could be affected by the intensity of sunlight. The outdoor temperature was 30-35 °C and the intensity of sunlight was 9-13 $mWcm^{-2}$ from 11 am to 3 pm.

Subsequently, 5 mL of the aliquot of crystal violet dye solution were withdrawn at 30 minutes interval for 4 hours and the aliquot was centrifuged at 7800 rpm for 10 minutes to remove photocatalyst. Centrifugation was applied to separate ZnO NPs from degraded dye solution so that dispersion of nanoparticles could be prevented. Presence of nanoparticles in the sample should be avoided as absorbance would be influenced due to scattering and absorption of nanoparticles.

The extent of crystal violet dye degradation was monitored by using UV-visible spectroscopy. The absorbance of aliquot collected at different time interval was measured at 583 nm which was the maximum wavelength of crystal violet dye. The percentage of dye degradation could be calculated using Equation 3.5 (Karimi, et al., 2014).

$$Percentage\ of\ dye\ degradation = \frac{A_0 - A_t}{A_0} \times 100\ \%\ \text{(Eq. 3.5)}$$

where A_0 = initial absorbance of dye solution, A_t = absorbance of dye solution at different time interval

CHAPTER 4

RESULTS AND DISCUSSION

4.1 Qualitative Phytochemical Screening

Qualitative phytochemical screening was executed to detect the presence of phytochemicals in peppermint tea dregs extract which acted as reducing agents, stabilising agents or capping agents in the synthesis of zinc oxide nanoparticles. The tests included Dragendorff's test and Wagner's test (test for alkaloids), alkaline reagent test and lead acetate test (test for flavonoids), foam test (test for saponins), ferric chloride test (test for tannins), Keller Killiani test (test for glycosides) and xanthoproteic test (test for proteins).

The test solutions for phytochemical screening were prepared by dissolving the peppermint tea dregs extract in ethanol in a ratio of 1:10. Figure 4.1.1 shows a test solution prepared.

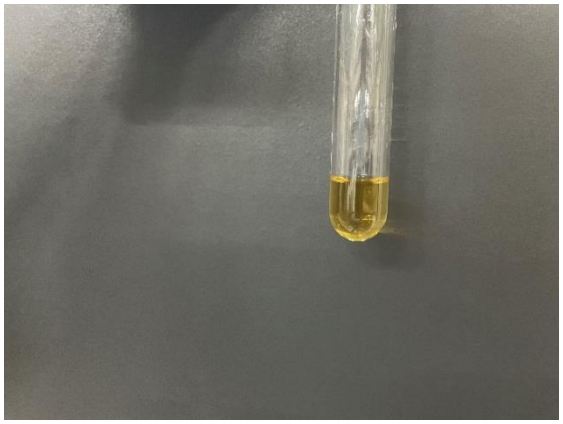

Figure 4.1.1: Test solution prepared by dissolving the peppermint tea dregs extract in ethanol in a ratio of 1:10

4.1.1 Test for Alkaloids

Dragendorff's test and Wagner's test were used to determine the presence of alkaloids in peppermint tea dregs extract. Both tests indicated the absence of alkaloids.

4.1.1.1 Dragendorff's Test

In Dragendorff's test, the light brown colour of peppermint tea dregs extract turned into orange after adding with a few drops of Dragendorff's reagent. However, no precipitate was formed in the solution as shown in Figure 4.1.2, implied that alkaloids was absent in the crude extract.

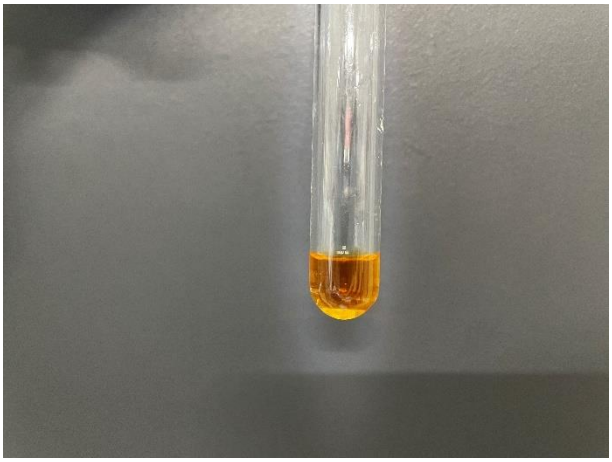

Figure 4.1.2: Observation of peppermint tea dregs extract in Dragendorff's test

4.1.1.2 Wagner's Test

When Wagner's reagent was added into the peppermint tea dregs extract, the light brown colour of crude extract turned reddish-brown, but no precipitate was formed as shown in Figure 4.1.3 further proved the absence of alkaloids in the crude extract.

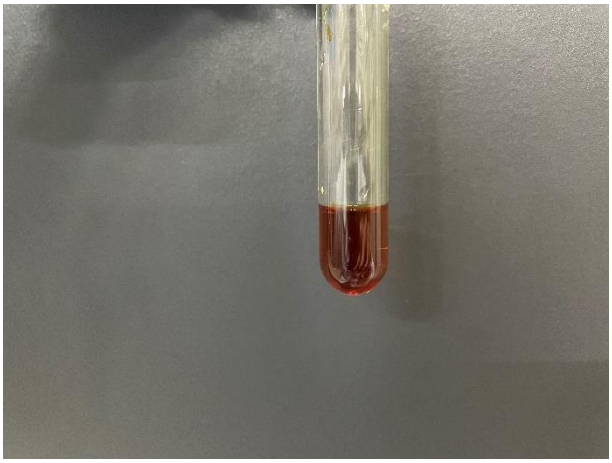

Figure 4.1.3: Observation of peppermint tea dregs extract in Wagner's test

4.1.2 Test for Flavonoids

To detect the existence of flavonoids, alkaline reagent test and lead acetate test were utilised. Both tests implied that the peppermint tea dregs extract contained flavonoids.

4.1.2.1 Alkaline Reagent Test

In this test, the test solution turned yellow after adding two to three drops of 1 M sodium hydroxide as shown in Figure 4.1.4.

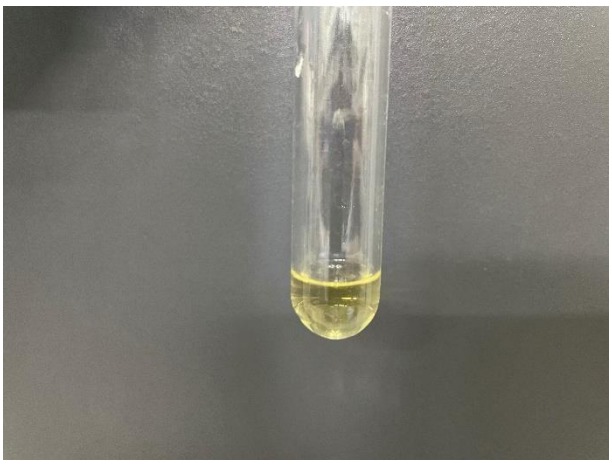

Figure 4.1.4: Observation of peppermint tea dregs extract after adding sodium hydroxide in alkaline reagent test

Next, the introduction of a few drops of dilute acetic acid caused the decolourisation of the test solution as observed in Figure 4.1.5. This had confirmed the presence of flavonoids in the peppermint tea dregs extract.

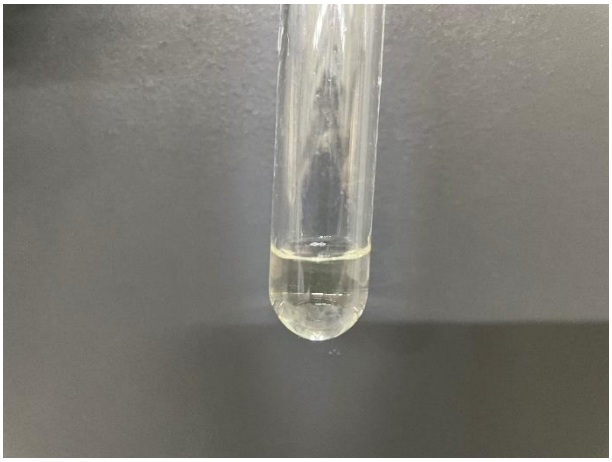

Figure 4.1.5: Observation of peppermint tea dregs extract after adding dilute acetic acid in alkaline reagent test

4.1.2.2 Lead Acetate Test

The existence of flavonoids in the peppermint tea dregs extract was further proved by lead acetate test. The appearance of precipitate in the test solution after adding a little amount of 10 % lead acetate as shown in Figure 4.1.6 implied the presence of flavonoids.

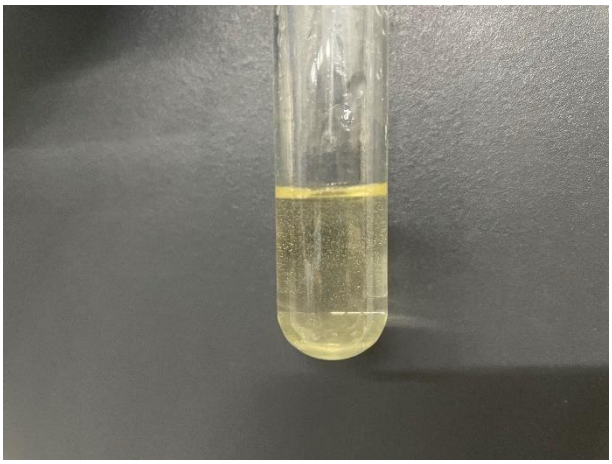

Figure 4.1.6: Observation of peppermint tea dregs extract in lead acetate test

4.1.3 Test for Saponins

In foam test, after shaking the peppermint tea dregs extract vigorously, foam was formed as illustrated in Figure 4.1.7. However, the foam was not able to persist for over a minute. As a result, it was claimed that the crude extract of peppermint tea dregs did not contain saponins.

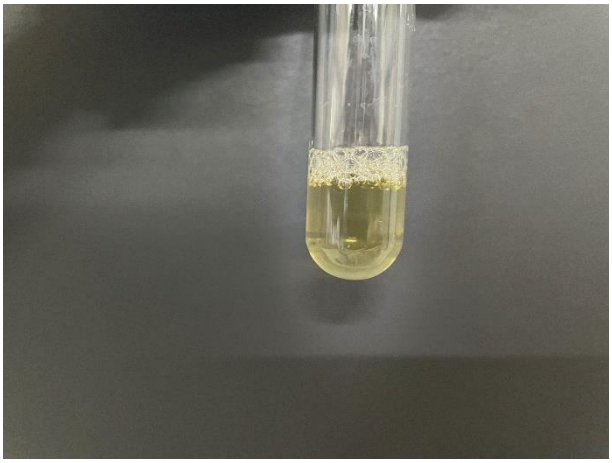

Figure 4.1.7: Observation of peppermint tea dregs extract after shaking in foam test

4.1.4 Test for Tannins

Ferric chloride test was carried out to detect tannins. As seen in Figure 4.1.8, the colour of the test solution did not change to blue green and no precipitate was formed when the peppermint tea dregs extract was treated with 5 % ferric(II) chloride. This had indicated the absence of tannins.

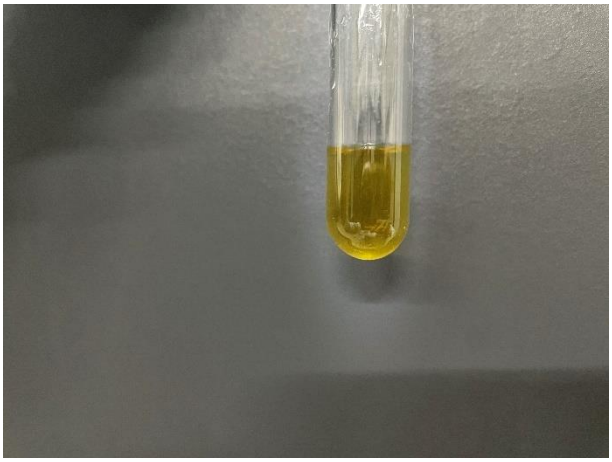

Figure 4.1.8: Observation of peppermint tea dregs extract in ferric chloride test

4.1.5 Test for Glycosides

In Keller Killiani test, there was no difference in the peppermint tea dregs extract before and after adding ferric(III) chloride, glacial acetic acid and concentrated sulphuric acid. Therefore, it was revealed that the crude extract did not contain glycosides.

4.1.6 Test for Proteins

The presence of proteins in peppermint tea dregs extract was determined by xanthoproteic test. Nevertheless, the crude extract showed no distinction before and after treating with concentrated nitric acid. Thus, it was concluded that proteins was absent in the crude extract.

4.1.7 Summary of Phytochemical Screening

Based on the results obtained from the qualitative phytochemical screening, the phytochemical that present in the peppermint tea dregs extract was flavonoids while alkaloids, saponins, tannins, proteins and glycosides were absent in the extract. Table 4.1.1 summarises the results obtained from the qualitative phytochemical screening of peppermint tea dregs extract.

Table 4.1.1: Summary of phytochemical screening of peppermint tea dregs extract

Chemical Constituent	Test	Result	
		Positive	Negative
Alkaloids	Dragendorff's test		×
	Wagner's test		×
Flavonoids	Alkaline reagent test	×	
	Lead acetate test	×	
Saponins	Foam test		×
Tannins	Ferric chloride test		×
Glycosides	Keller Killiani test		×
Proteins	Xanthoproteic test		×

4.2 Characterisation of Peppermint Tea Dregs Extract

The resulting peppermint tea dregs extract appeared in light brown colour. It was served as the reducing agent and stabilising agent in the synthesis of zinc oxide nanoparticles.

4.2.1 Fourier Transform Infrared Spectroscopy (FTIR)

To determine the functional groups present in the peppermint tea dregs extract, the extract was freeze dried into solid for FTIR analysis. According to the infrared spectrum shown in Figure 4.2.1, there was an intense peak at 3435 cm^{-1} which could be assigned to the presence of O-H stretching vibration, indicating the phenolic group. The spectrum showed a sharp peak at 1637 cm^{-1} which revealed the C=O or C=C stretching vibration, showing the presence of carbonyl group or aromatic group. The peak at 1384 cm^{-1} was due to the COO^- stretch. Besides, C-O stretching vibrations appeared at 1259 cm^{-1} and 1074 cm^{-1}. Peak generated at 621 cm^{-1} was likely owing to the weak reflectance in biomass, implying the presence of assorted oxides and symmetrical S-O vibrations that would appear in between 1000-450 cm^{-1} and 700-610 cm^{-1} respectively (Mishra, et al., 2010). All the peaks observed could be correlated to the structure of flavonoids that are the naturally occurring phenolic compounds (Sulaiman and Balachandran, 2012).

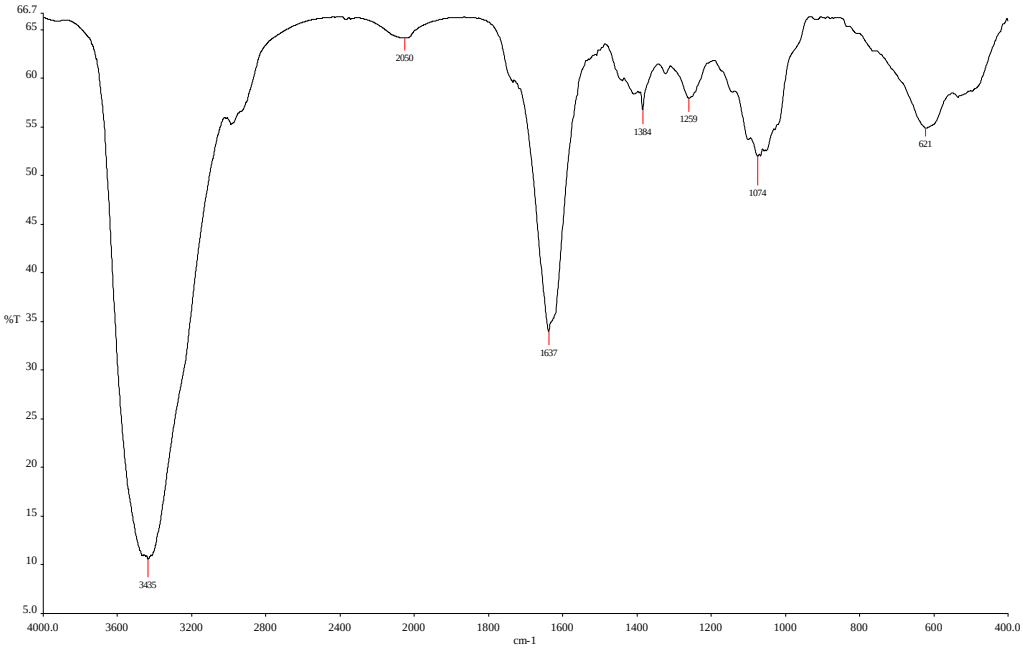

Figure 4.2.1: FTIR spectrum of peppermint tea dregs extract

4.3 Yield of Synthesised Zinc Oxide Nanoparticles

The influences of mass of zinc nitrate hexahydrate and calcination temperature on the yield of synthesised zinc oxide nanoparticles were studied. In this study, there was a total of seven procedures conducted.

The yield and percent yield calculated from Equation 3.1 of each synthesised zinc oxide nanoparticles using different mass of zinc nitrate hexahydrate are tabulated in Table 4.3.1.

Table 4.3.1: Yield and percent yield of each ZnO NPs synthesised using different mass of $Zn(NO_3)_2.6H_2O$ at 450 °C

Mass of zinc nitrate hexahydrate used (g)	Mass of ZnO NPs synthesised (g)	Percent yield of ZnO NPs synthesised (%)
5	1.1134	22.27
10	1.9612	19.61
15	3.0386	20.26
20	4.3115	21.56

From Table 4.3.1, it was observed that increasing mass of zinc nitrate hexahydrate used could increase the yield of ZnO NPs synthesised. However, the percent yield of ZnO NPs calculated had no big difference among all. Thus, it was concluded that the mass of zinc nitrate hexahydrate used would affect the yield but would not affect the precent yield of ZnO NPs synthesised.

Table 4.3.2 records the yield and percent yield of each synthesised zinc oxide nanoparticles using different calcination temperature.

Table 4.3.2: Yield and percent yield of each ZnO NPs synthesised using 5 g of $Zn(NO_3)_2.6H_2O$ at different calcination temperature

Calcination temperature (°C)	Mass of ZnO NPs synthesised (g)	Percent yield of ZnO NPs synthesised (%)
450	1.1134	22.27
550	1.1178	22.36
650	1.0979	21.96
750	1.1776	23.55

From Table 4.3.2, it was found that the ZnO NPs synthesised at different calcination temperature had not much difference in terms of yield and percent yield. Hence, it was deduced that the yield and precent yield of ZnO NPs synthesised would not be affected by the calcination temperature.

4.4 Characterisation of Zinc Oxide Nanoparticles

The green synthesis of zinc oxide nanoparticles was accomplished using peppermint tea dregs extract as a natural agent. Zinc nitrate hexahydrate was served as the metal precursor for bottom-up approach of nanoparticles synthesis and the solvent used was deionised water.

During the synthesis, the peppermint tea dregs extract was added with zinc nitrate hexahydrate and the mixture was maintained at 70-80 °C with constant stirring to dissolve the salt homogenously and to accelerate the reaction. 70-

80 °C was used to prevent the phytochemicals in the extract from decomposing at higher temperatures. Upon continuous heating, the colour of the extract slowly turned into darker brown from a lighter brown. Heating was stopped when brown paste was obtained as a result of concentration by solvent evaporation. The brown paste was proceeded to calcination in the furnace for 2 hours to form the final product, zinc oxide nanoparticles. Calcination promoted the oxygen binding, biomolecules decomposition and uniform nano-sized particles crystallisation (Messing, 2021).

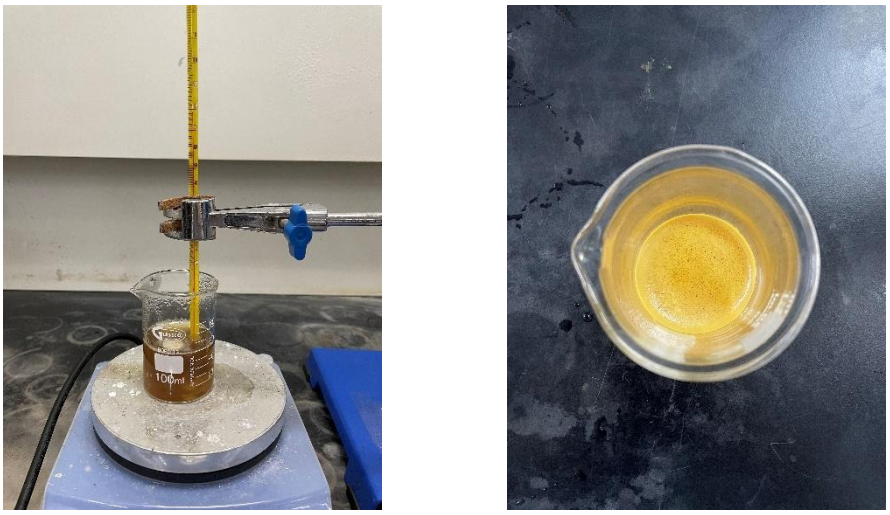

Figure 4.4.1: Peppermint tea dregs extract and brown paste obtained

The colour of zinc oxide nanoparticles synthesized by peppermint tea dregs extract using different mass of zinc nitrate hexahydrate and different calcination temperature was yellowish-white as shown in Figure 4.4.2.

Figure 4.4.2: Zinc oxide nanoparticles synthesised

Later, the synthesised zinc oxide nanoparticles were characterised and elucidated via various analytical techniques such as Fourier transform infrared spectroscopy (FTIR), ultraviolet-visible spectroscopy (UV-Vis), X-ray diffraction (XRD), field emission scanning electron microscopy (FESEM), energy dispersive X-ray analysis (EDX) and particle size analysis (PSA).

4.4.1 Fourier Transform Infrared Spectroscopy (FTIR)

Fourier transform infrared spectroscopy was utilised to recognise the functional groups present in the zinc oxide nanoparticles synthesised particularly the absorption peak of Zn-O bonding to prove the product formed was indeed the zinc oxide nanoparticles.

Figures 4.4.3-4.4.6 show the infrared spectra of zinc oxide nanoparticles synthesised from different mass of zinc nitrate hexahydrate while other

parameters remained the same. The mass of zinc nitrate hexahydrate investigated were 5 g, 10 g, 15 g and 20 g. The intense peak at 3436 cm^{-1} indicated the O-H stretching vibration and its intensity increased drastically as mass of zinc nitrate hexahydrate increased. There was a weak peak at 2974 cm^{-1} which could be attributed to the C-H stretching vibration, but this peak disappeared when greater mass of zinc nitrate hexahydrate was used. The spectrum showed a peak at around 1638 cm^{-1} which revealed the C=O or C=C stretching vibration, showing the presence of carbonyl group or aromatic group. This peak intensity was linearly proportional to the mass of zinc nitrate hexahydrate. Furthermore, the sharp peak of COO^- stretch appeared at 1384 cm^{-1} and the intensity of this peak reduced as mass of zinc nitrate hexahydrate used increased. Apart from that, the strong peak generated at around 449 cm^{-1} implied the Zn-O stretching vibration, but the peak became broader and less intense as mass of zinc nitrate hexahydrate used increased. This might be due to more types of ZnO NPs were formed resulting from the highly concentrated zinc nitrate hexahydrate. Another possible reason could be attributed to the strong intermolecular interactions of the Zn-O bond.

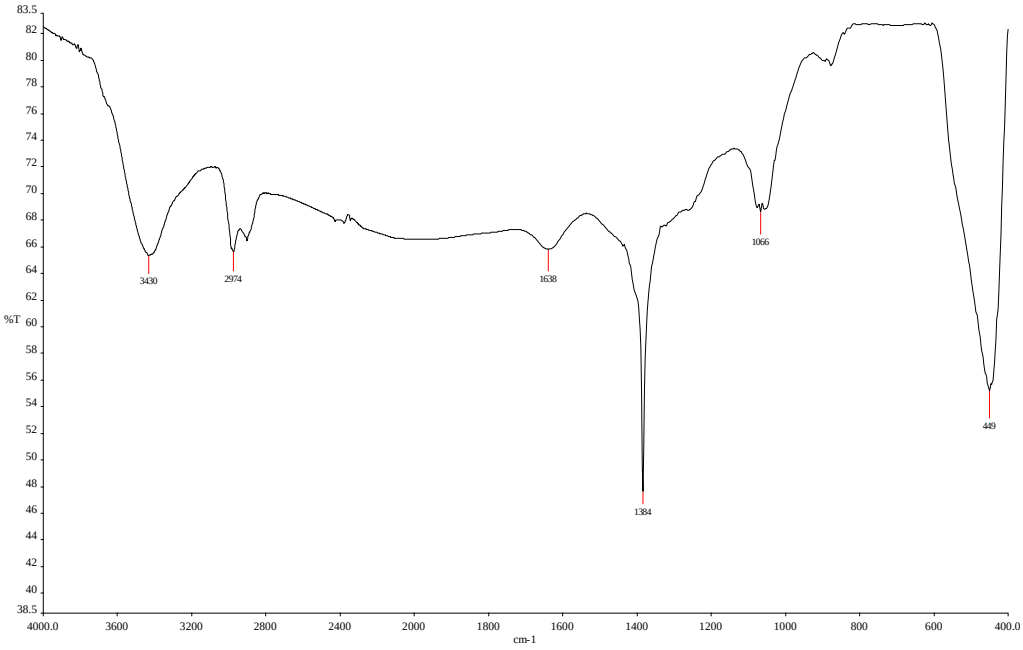

Figure 4.4.3: FTIR spectrum of ZnO NPs synthesised from 5 g of $Zn(NO_3)_2.6H_2O$ at 450 °C

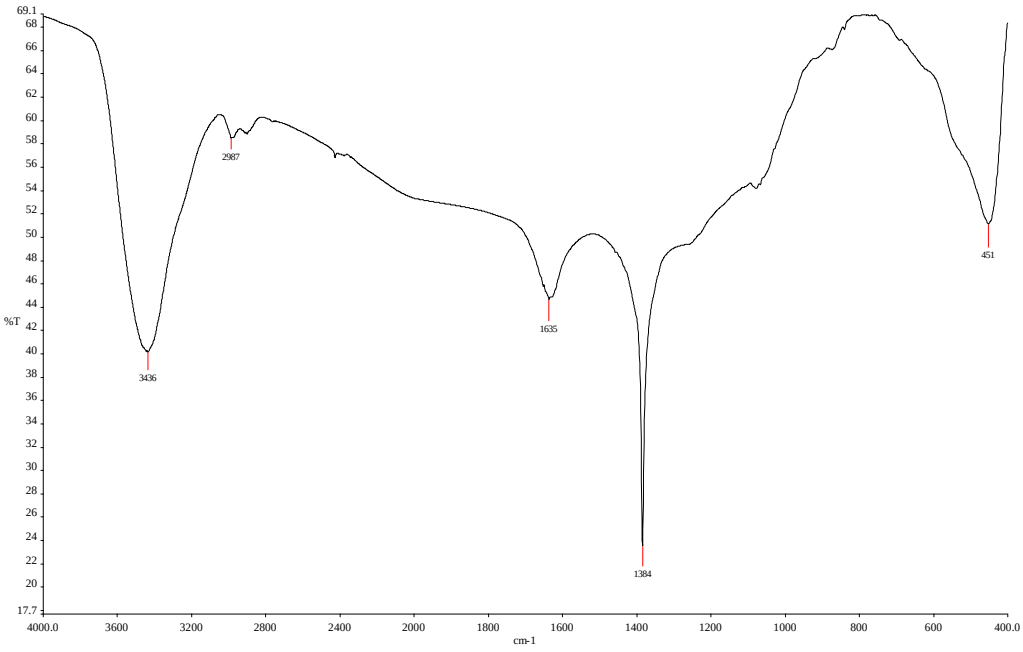

Figure 4.4.4: FTIR spectrum of ZnO NPs synthesised from 10 g of $Zn(NO_3)_2.6H_2O$ at 450 °C

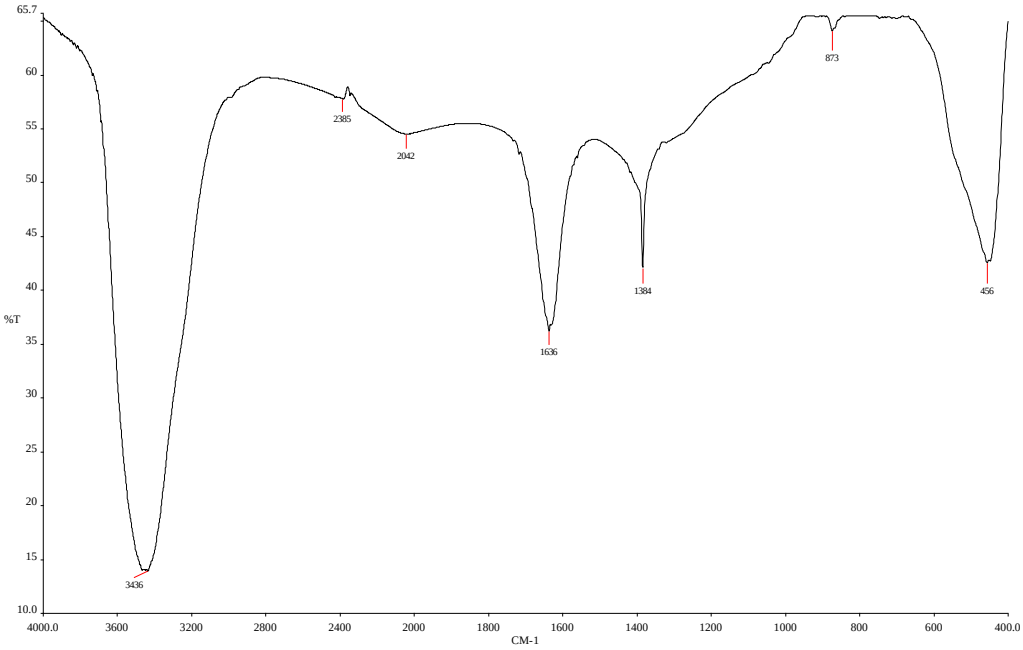

Figure 4.4.5: FTIR spectrum of ZnO NPs synthesised from 15 g of $Zn(NO_3)_2.6H_2O$ at 450 °C

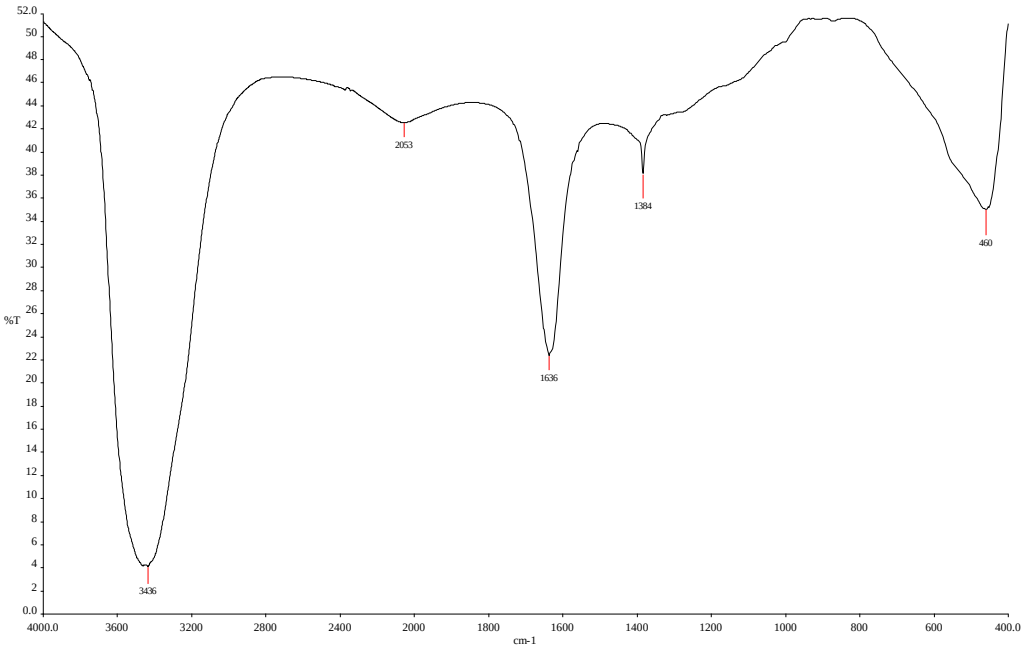

Figure 4.4.6: FTIR spectrum of ZnO NPs synthesised from 20 g of $Zn(NO_3)_2.6H_2O$ at 450 °C

Figures 4.4.7-4.4.10 show the infrared spectra of zinc oxide nanoparticles synthesised with the same conditions but at different calcination temperatures which were 450 °C, 550 °C, 650 °C and 750 °C respectively. There was an intense peak at around 3436 cm^{-1} which could be assigned to the O-H stretching vibration. The weak peak at 2987 cm^{-1} indicated the presence of C-H stretching vibration. Moreover, the spectrum showed a peak at around 1638 cm^{-1} which revealed the C=O or C=C stretching vibration, showing the presence of carbonyl group or aromatic group. Furthermore, the sharp peak appeared at 1384 cm^{-1} was due to the symmetrical stretching of the zinc carboxylate. Other than that, the peak generated at around 1066 cm^{-1} implied the C-O stretching vibration. Lastly, Zn-O stretching vibration was shown at around 449 cm^{-1}. Based on the results, the infrared spectra obtained showed similar pattern despite different calcination temperatures were used except that the Zn-O stretching vibration was the strongest when the ZnO NPs was calcinated at 450 °C. On top of that, at 450 °C calcination temperature, the intensity of peak 1384 cm^{-1} was the highest whereas the intensity of peak 1638 cm^{-1} and 3430 cm^{-1} were the lowest among four. This phenomenon occurred indicated that there were less bioactive compounds adsorbed on the surface of ZnO NPs synthesised at 450 °C.

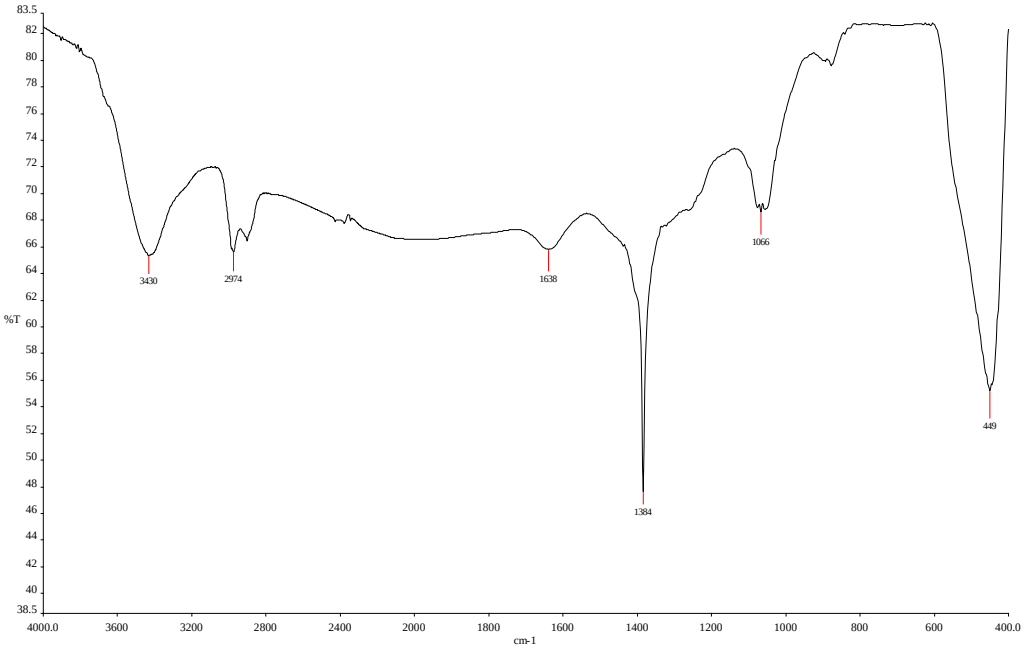

Figure 4.4.7: FTIR spectrum of ZnO NPs synthesised from 5 g of $Zn(NO_3)_2.6H_2O$ at 450 °C

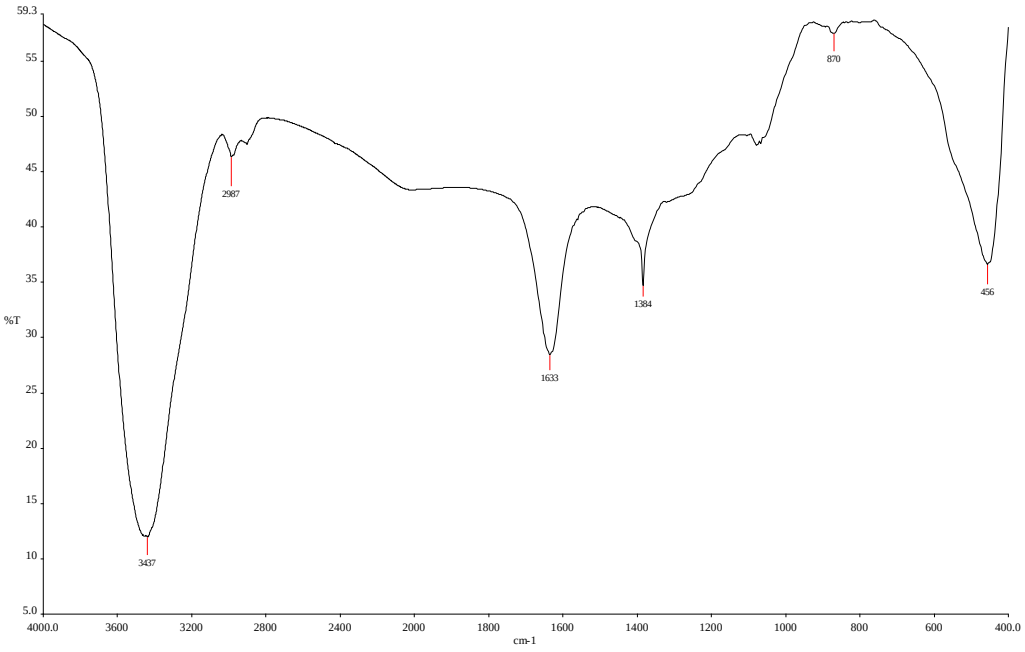

Figure 4.4.8: FTIR spectrum of ZnO NPs synthesised from 5 g of $Zn(NO_3)_2.6H_2O$ at 550 °C

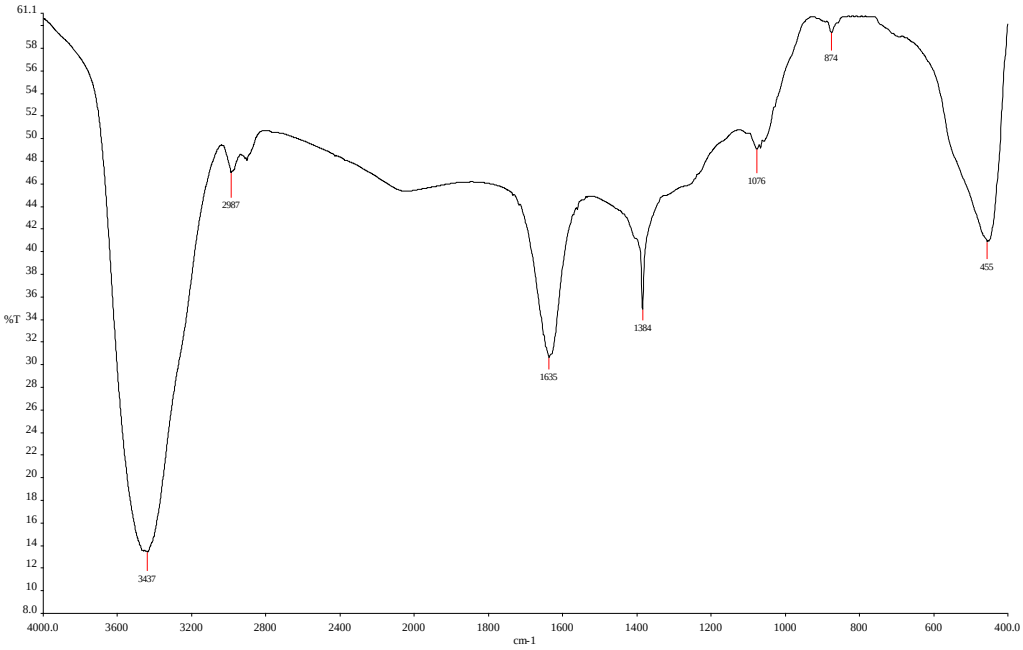

Figure 4.4.9: FTIR spectrum of ZnO NPs synthesised from 5 g of $Zn(NO_3)_2.6H_2O$ at 650 °C

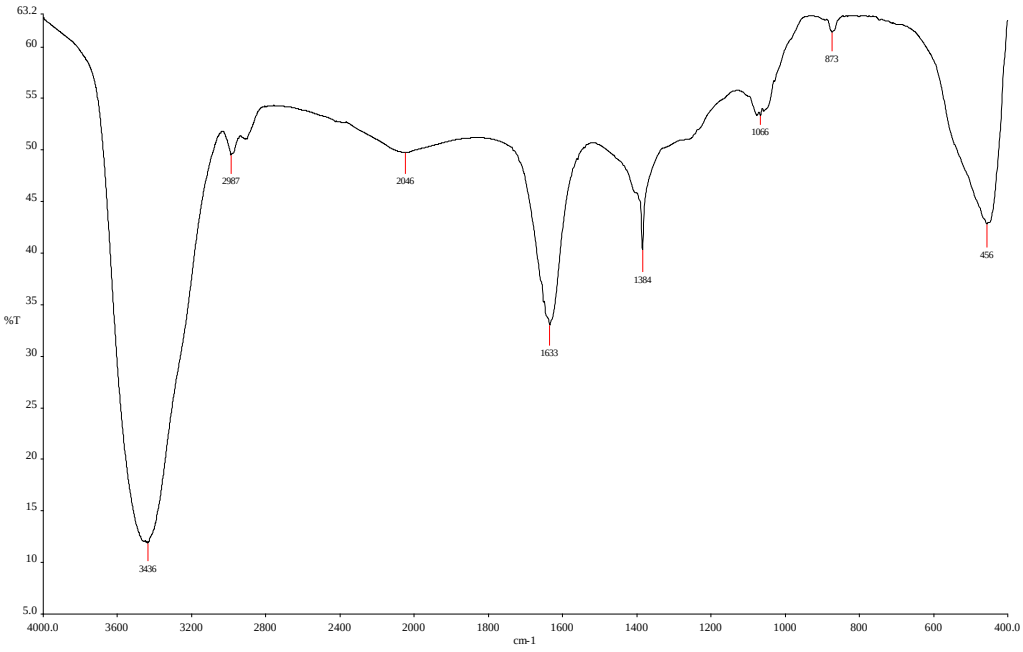

Figure 4.4.10: FTIR spectrum of ZnO NPs synthesised from 5 g of $Zn(NO_3)_2.6H_2O$ at 750 °C

By comparing all these infrared spectra of zinc oxide nanoparticles synthesised, it could be concluded that the ZnO NPs produced from 5 g of zinc nitrate hexahydrate and at 450 °C calcination temperature was the best since it had the strongest signal of Zn-O stretching vibration. By comparing the FTIR spectrum of ZnO NPs synthesised from 5 g of zinc nitrate hexahydrate at 450 °C with the FTIR spectrum of peppermint tea dregs extract, the ZnO NPs showed similar absorption peaks corresponding to the tea dregs extract, indicating that some bioactive compounds might be adsorbed on the ZnO NPs surface during the synthesis. One of the distinctions was some peaks observed in the extract went disappear in the ZnO NPs synthesised. Thermal decomposition or oxidation of biomolecules during the synthesis explain this finding, since EDX results had proved that the bioactive compounds would be thermally decomposed at higher temperatures. Another most significant variation was the presence of Zn-O absorption peak in the infrared spectrum of ZnO NPs, confirming the formation of zinc oxide nanoparticles.

4.4.2 Ultraviolet-Visible Spectroscopy (UV-Vis)

Ultraviolet-visible spectroscopy was utilised to determine the absorption value of zinc oxide nanoparticles in its characterisation. Absorption spectroscopy is a strong non-destructive tool for exploiting the optical properties of semiconducting nanoparticles. The UV-Vis spectra are a function of wavelength, and the maximum wavelength affects the size of nanoparticles. The band gap energy is determined by the energy difference between the conduction band and valence band (Mohammadian, et al., 2018).

According to Figure 4.4.11, the UV-Vis spectra of zinc oxide nanoparticles synthesised using 5 g, 10 g, 15 g and 20 g of zinc nitrate hexahydrate had shown the maximum absorption wavelength of ZnO NPs synthesised was 368 nm. This result is in line with the research of Mohammadian and his coworkers (2018) on the characteristic wavelength range of zinc oxide nanoparticles. Due to their high excitation binding energy at ambient temperature, the ZnO NPs had an exciton absorption peak at 361-368 nm. On the other hand, the ZnO NPs synthesised at calcination temperatures of 550 °C, 650 °C and 750 °C showed no peak on the UV-Vis spectra. This was due to the agglomeration of ZnO NPs, resulting in the inability of ZnO NPs to disperse well in the solution. All the particles sank to the bottom of the cuvette during the UV-Vis analysis. Therefore, the UV-Vis spectrophotometer could not detect any analyte.

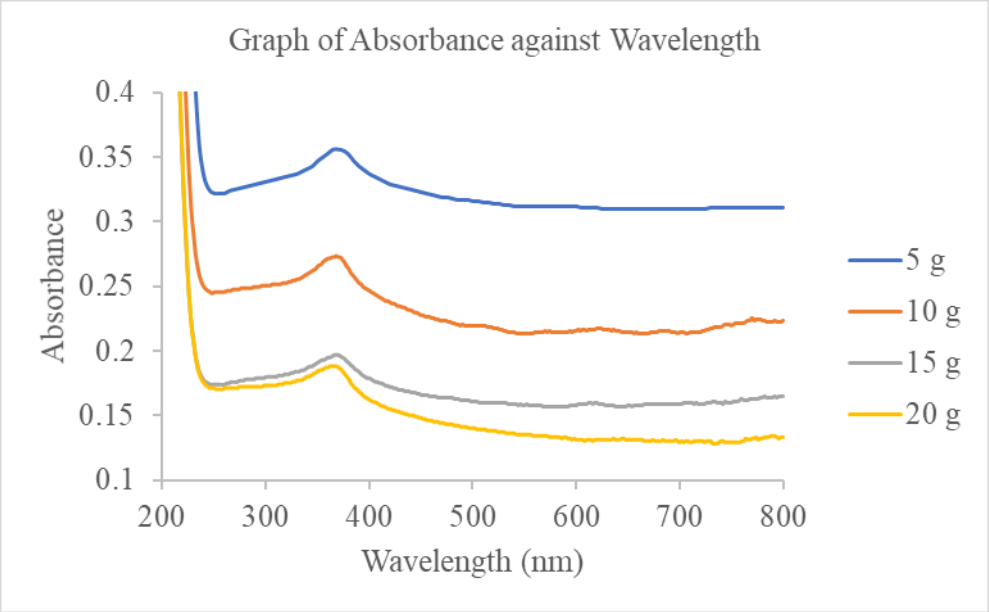

Figure 4.4.11: UV-Vis spectra of ZnO NPs synthesised using different mass of $Zn(NO_3)_2.6H_2O$

The energy difference between the bound and free states, between the valence and conduction bands, referred to as band gap energy. Thus, the band gap is the minimum energy change needed to excite an electron and allow it to participate in conduction (Honsberg and Bowden, 2022). The band gap energy could be calculated from the maximum absorption wavelength of the synthesised ZnO NPs. By using Equation 3.2, the band gap energy of the zinc oxide nanoparticles synthesised was 3.37 eV which is in accordance with the literature. This had confirmed that the product formed was truly zinc oxide nanoparticles.

The synthesised ZnO NPs had a higher band gap energy than the bulk ZnO that had a band gap of 2.98 eV (Opoku, et al., 2017). Another research by Nawaz and his co-workers (2011) had shown that bulk ZnO had a maximum wavelength at 388 nm, which correlated to 3.20 eV of band gap energy. The blue shift behaviour of maximum absorption is compatible with the increment of band gap energy from bulk materials to nanoparticles since higher energy results in lower wavelength. Because of the property of Surface Plasmon Resonance, the absorption peak of nanoparticles shifted to lower wavelength or higher energy, resulting in reducing size (Gupta, et al., 2015). This is due to the quantum confinement effect that resulted from the decreasing in size of zinc oxide nanoparticles (Nawaz, et al., 2011). As the particle size decreases, the energy level becomes discrete, explained in Figure 4.4.12.

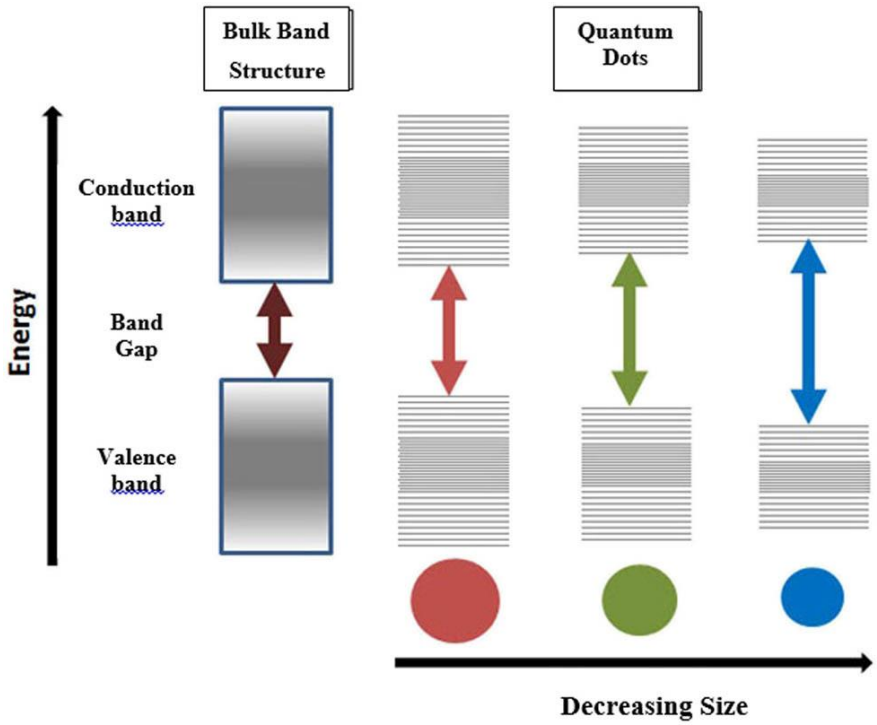

Figure 4.4.12: Illustration of quantum confinement effect (Mohamed, et al., 2021)

The binding of oxygen and shrinking in size from bulk caused the absorption of ZnO NPs to occur at a shorter wavelength. Consequently, the ZnO NPs could be potentially utilised as a photocatalyst in the presence of oxygen, allowing the oxidation of organic molecules in response to solar energy activation.

4.4.3 X-Ray Diffraction (XRD)

To determine the crystallinity of zinc oxide nanoparticles synthesised from peppermint tea dregs extract, X-ray diffraction was used. In the XRD spectra

obtained, the peaks were accredited to (100), (002), (101), (102), (110), (103), (112) and (201) planes.

In Figure 4.4.13, the zinc oxide nanoparticles synthesised using 5 g of zinc nitrate hexahydrate had distinct peaks of diffraction at 2θ position with the values of 31.77°, 34.43°, 36.26°, 47.55°, 56.60°, 62.87°, 67.96°, 69.10°. The relative pattern of the synthesized ZnO NPs was 93.9 % matched with ICDD 01-070-2551 with hexagonal wurtzite structure of ZnO NPs in terms of the intensity and position. By using the Debye-Scherrer's equation, the average crystallite size was calculated to be 47.23 nm.

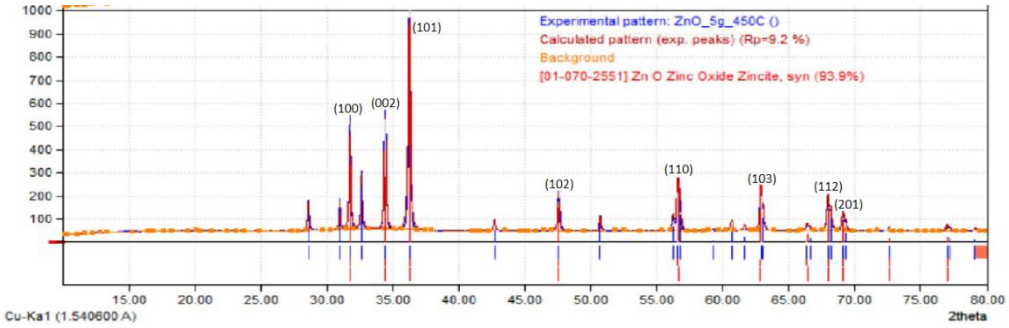

Figure 4.4.13: XRD spectrum of ZnO NPs synthesised using 5 g of $Zn(NO_3)_2.6H_2O$ at 450 °C

In Figure 4.4.14, zinc oxide nanoparticles synthesised using 10 g of zinc nitrate hexahydrate had distinct peaks of diffraction at 2θ position with the values of 31.77°, 34.43°, 36.26°, 47.55°, 56.60°, 62.87°, 67.96°, 69.09°. The relative pattern of the synthesized ZnO NPs was 94.1 % matched with ICDD 01-070-2551 with hexagonal wurtzite structure of ZnO NPs in terms of the intensity

and position. By using the Debye-Scherrer's equation, the average crystallite size was calculated to be 48.18 nm.

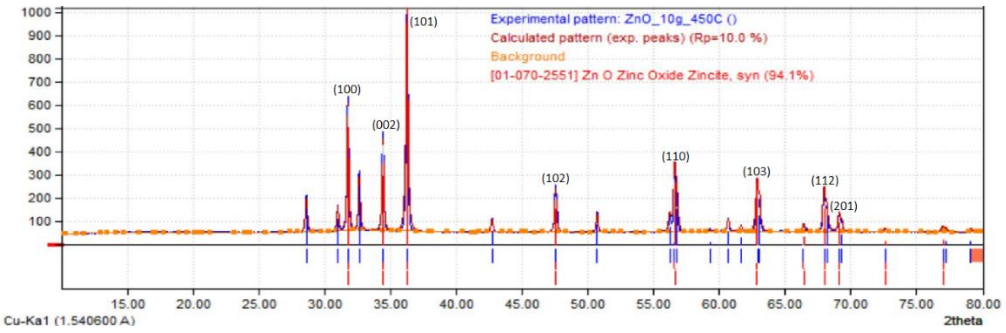

Figure 4.4.14: XRD spectrum of ZnO NPs synthesised using 10 g of $Zn(NO_3)_2.6H_2O$ at 450 °C

In Figure 4.4.15, the zinc oxide nanoparticles synthesised using 15 g of zinc nitrate hexahydrate had distinct peaks of diffraction at 2θ position with the values of 31.78°, 34.44°, 36.27°, 47.56°, 56.61°, 62.88°, 67.97°, 69.11°. The relative pattern of the synthesized ZnO NPs was 94.1 % matched with ICDD 01-078-4493 with hexagonal wurtzite structure of ZnO NPs in terms of the intensity and position. By using the Debye-Scherrer's equation, the average crystallite size was calculated to be 53.34 nm.

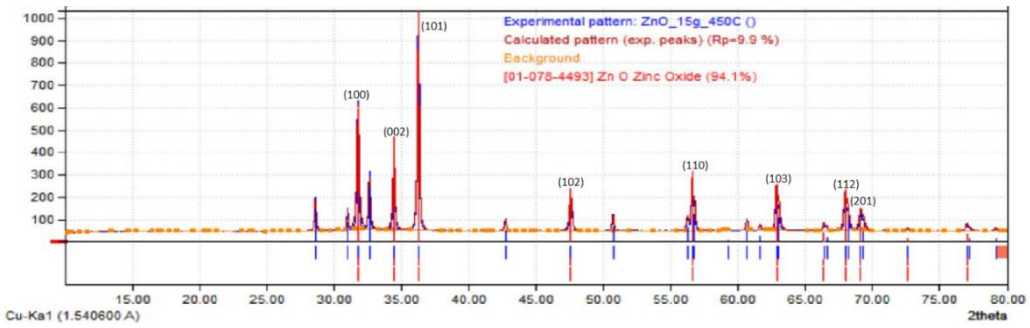

Figure 4.4.15: XRD spectrum of ZnO NPs synthesised using 15 g of $Zn(NO_3)_2.6H_2O$ at 450 °C

In Figure 4.4.16, the zinc oxide nanoparticles synthesised using 20 g of zinc nitrate hexahydrate had distinct peaks of diffraction at 2θ position with the values of 31.78°, 34.44°, 36.27°, 47.56°, 56.61°, 62.88°, 67.97°, 69.10°. The relative pattern of the synthesized ZnO NPs was 94.4 % matched with ICDD 01-074-9939 with hexagonal wurtzite structure of ZnO NPs in terms of the intensity and position. By using the Debye-Scherrer's equation, the average crystallite size was calculated to be 49.94 nm.

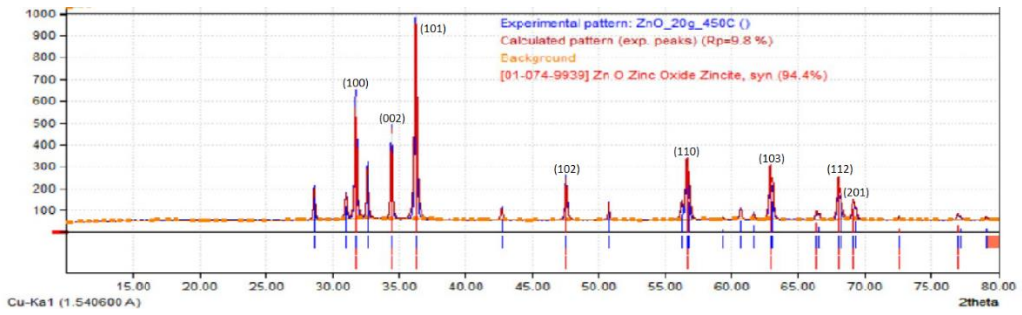

Figure 4.4.16: XRD spectrum of ZnO NPs synthesised using 20 g of $Zn(NO_3)_2.6H_2O$ at 450 °C

In Figure 4.4.17, the synthesised zinc oxide nanoparticles calcinated at 550 °C had distinct peaks of diffraction at 2θ position with the values of 31.77°, 34.43°, 36.26°, 47.55°, 56.60°, 62.87°, 67.96°, 69.10°. The relative pattern of the synthesized ZnO NPs was 94.1 % matched with ICDD 01-070-2551 with hexagonal wurtzite structure of ZnO NPs in terms of the intensity and position. By using the Debye-Scherrer's equation, the average crystallite size was calculated to be 46.14 nm.

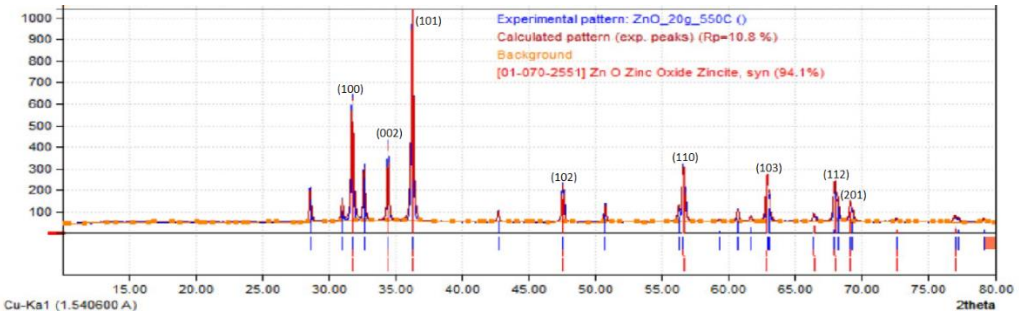

Figure 4.4.17: XRD spectrum of ZnO NPs synthesised using 5 g of $Zn(NO_3)_2.6H_2O$ at 550 °C

In Figure 4.4.18, the synthesised zinc oxide nanoparticles calcinated at 650 °C had distinct peaks of diffraction at 2θ position with the values of 31.78°, 34.44°, 36.27°, 47.56°, 56.61°, 62.88°, 67.97°, 69.11°. The relative pattern of the synthesized ZnO NPs was 94.1 % matched with ICDD 01-089-7102 with hexagonal wurtzite structure of ZnO NPs in terms of the intensity and position. By using the Debye-Scherrer's equation, the average crystallite size was calculated to be 53.22 nm.

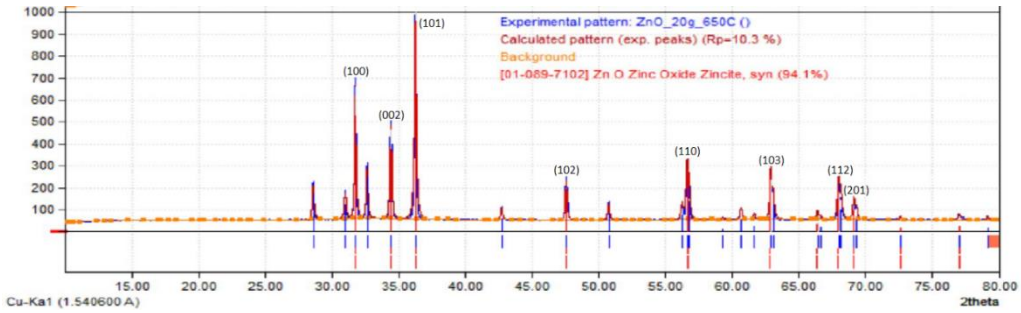

Figure 4.4.18: XRD spectrum of ZnO NPs synthesised using 5 g of $Zn(NO_3)_2.6H_2O$ at 650 °C

In Figure 4.4.19, the synthesised zinc oxide nanoparticles calcinated at 750 °C had distinct peaks of diffraction at 2θ position with the values of 31.77°, 34.44°, 36.27°, 47.55°, 56.60°, 62.87°, 67.96°, 69.10°. The relative pattern of the synthesized ZnO NPs was 94.0 % matched with ICDD 01-070-2551 with hexagonal wurtzite structure of ZnO NPs in terms of the intensity and position. By using the Debye-Scherrer's equation, the average crystallite size was calculated to be 52.76 nm.

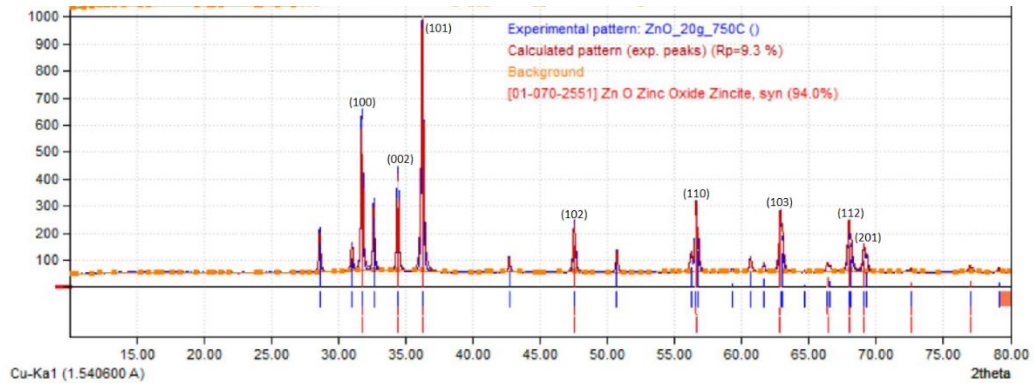

Figure 4.4.19: XRD pattern of ZnO NPs synthesised using 5 g of $Zn(NO_3)_2.6H_2O$ at 750 °C

In another research conducted by Ahmad and his co-workers (2019), the distinct diffraction peaks at 2θ position were 31.717°, 34.484°, 36.245°, 47.585°, 56.705°, 62.826°, 68.025°, 69.039° which corresponded to the crystal lattice planes of (100), (002), (101), (102), (110), (103), (112) and (201) respectively. The XRD spectra obtained in this research were almost matched with their results in terms of intensities and positions. This confirmed the samples were indeed zinc oxide nanoparticles.

Well crystalline nature of zinc oxide was indicated by the high intense diffraction peaks. The high intensity at peak (101) indicated anisotropic development, implying on a preferred orientation of the crystallites (Ahmad, et al., 2019). However, there were some unrelated peaks which might be due to some impurities on the samples that came from the remaining of phytochemicals in the peppermint tea dregs extract. Generally, the average crystallite size increased when the mass of zinc nitrate hexahydrate used increased and when the calcination temperature increased. This result is in accordance with the previous study conducted by Saravanan and his co-workers (2013).

4.4.4 Field Emission Scanning Electron Microscopy (FESEM)

The function of field emission scanning electron microscopy (FESEM) is to determine the morphology as well as particle shape and size range of zinc oxide nanoparticles synthesised.

Figure 4.4.20(A) displays the FESEM image at 60,000x magnification of zinc oxide nanoparticles synthesised using 5 g of zinc nitrate hexahydrate at 450 °C calcination temperature. It could be observed that the particles synthesised were irregularly shaped spherical with a dimension ranging from 20.0 nm to 35.0 nm.

Figure 4.4.20(B) displays the FESEM image at 60,000x magnification of zinc oxide nanoparticles synthesised using 10 g of zinc nitrate hexahydrate at 450 °C calcination temperature. It could be observed that the particles synthesised were irregularly shaped spherical with a dimension ranging from 20.0 nm to 55.0 nm.

Figure 4.4.20(C) displays the FESEM image at 60,000x magnification of zinc oxide nanoparticles synthesised using 15 g of zinc nitrate hexahydrate at 450 °C calcination temperature. It could be observed that the particles synthesised were irregularly shaped longitudinal with a dimension ranging from 30.0 nm to 45.0 nm.

Figure 4.4.20(D) displays the FESEM image at 60,000x magnification of zinc oxide nanoparticles synthesised using 20 g of zinc nitrate hexahydrate at 450 °C calcination temperature. It could be observed that the particles synthesised were irregularly shaped spherical with a dimension ranging from 15.0 nm to 45.0 nm.

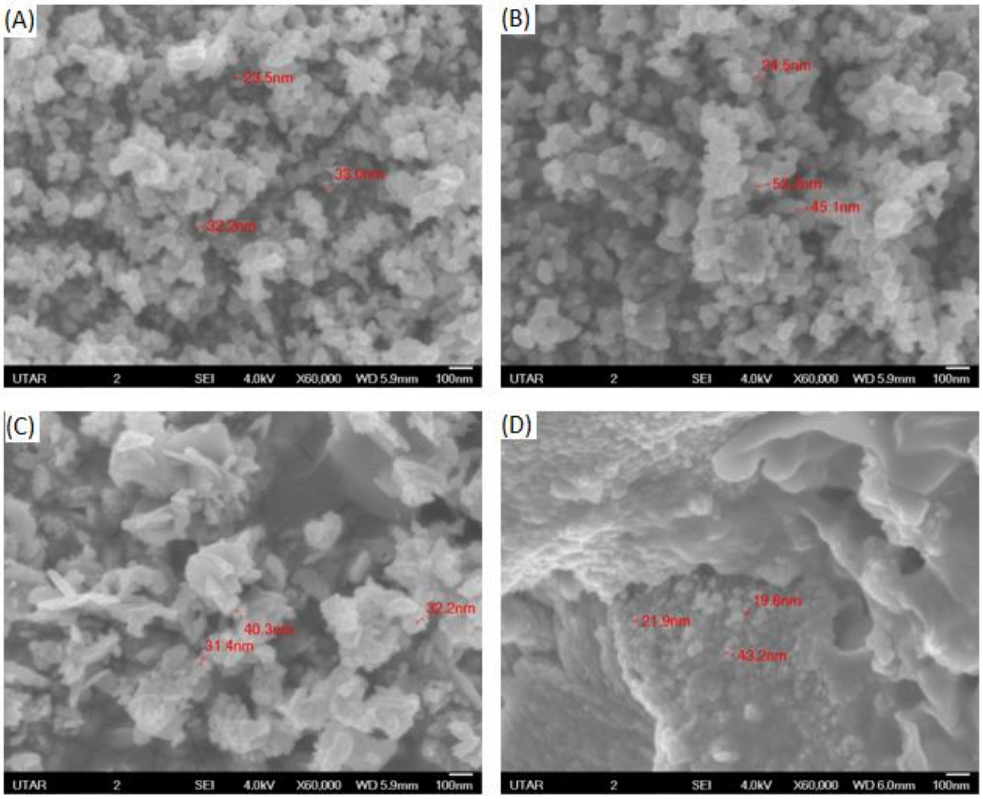

Figure 4.4.20: FESEM images at 60,000x magnification of ZnO NPs synthesised using (A) 5 g, (B) 10 g, (C) 15 g and (D) 20 g of $Zn(NO_3)_2.6H_2O$ at 450 °C

Figure 4.4.21(A) displays the FESEM image at 30,000x magnification of zinc oxide nanoparticles synthesised using 5 g of zinc nitrate hexahydrate at 550 °C calcination temperature. It could be observed that the particles synthesised were irregular in shape with a dimension ranging from 40.0 nm to 70.0 nm.

Figure 4.4.21(B) displays the FESEM image at 30,000x magnification of zinc oxide nanoparticles synthesised using 5 g of zinc nitrate hexahydrate at 650 °C calcination temperature. It could be observed that the particles synthesised were irregular in shape with a dimension ranging from 50.0 nm to 220.0 nm.

Figure 4.4.21(C) displays the FESEM image at 30,000x magnification of zinc oxide nanoparticles synthesised using 5 g of zinc nitrate hexahydrate at 750 °C calcination temperature. It could be observed that the particles synthesised were irregularly shaped hexagonal with all the particles stacked together.

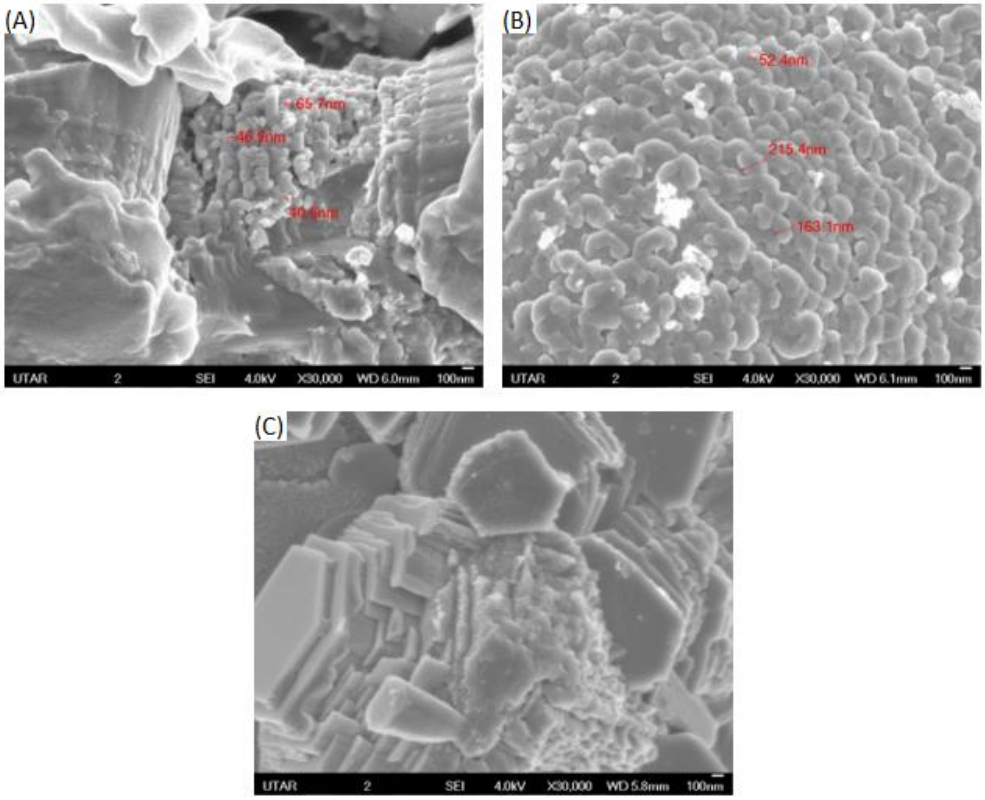

Figure 4.4.21: FESEM images at 30,000x magnification of ZnO NPs synthesised using 5 g of $Zn(NO_3)_2.6H_2O$ at (A) 550 °C, (B) 650 °C and (C) 750 °C

Based on the FESEM images, the phenomena of agglomeration were clearly observed in every ZnO NPs synthesised regardless of the mass of zinc nitrate hexahydrate used or the calcination temperature. This happened due to the absence of alkaloids in the peppermint tea dregs extract, as proven in the

qualitative phytochemical screening of the extract. Alkaloids serve as the stabilising agent (Adelere and Lateef, 2016; Din, et al., 2021) or capping agent (Shaheen and Ahmad, 2020) in the synthesis of metallic nanoparticles, preventing the particle agglomeration and helping in tuning the size and shape of nanoparticles. Hence, without alkaloids, the ZnO NPs synthesised agglomerated. The interparticle repulsive force or the electrostatic force was another reason why the ZnO NPs clumped together (Kulkarni, et al., 2003). The agglomeration phenomena extended with increasing mass of zinc nitrate hexahydrate used and with increasing calcination temperature.

Additionally, the size of synthesised ZnO NPs increased with increasing mass of zinc nitrate hexahydrate used and with increasing calcination temperature as well. This event worsened when the calcination temperature was at 650 °C and 750 °C, in which forming ZnO out of nanoscale. Gupta and his co-workers (2015) also reported that a hexagon-like ZnO had a larger particle size as compared to other shapes. This might explain why no peak was observed in their UV-Vis spectra. This result is consistent with previous study conducted by Muruganandham and his co-workers (2009), in which at higher temperatures, the size of nanoparticles increased, and the degree of agglomeration increased with increasing temperature as well. On that account, the zinc oxide nanoparticles synthesised using 5 g of zinc nitrate hexahydrate at 450 °C calcination temperature was the greatest among all as it had the smallest particle size and least agglomeration.

4.4.5 Energy Dispersive X-Ray Analysis (EDX)

The elemental composition of zinc oxide nanoparticles synthesised was determined by EDX.

Figure 4.4.22(A) presents the EDX profile of zinc oxide nanoparticles synthesised using 5 g of zinc nitrate hexahydrate at calcination temperature of 450 °C. The EDX spectrum showed the presence of zinc with a weight percent of 40.92 %, oxygen with a weight percent of 25.68 % and carbon with a weight percent of 33.40 %.

Figure 4.4.22(B) presents the EDX profile of zinc oxide nanoparticles synthesised using 10 g of zinc nitrate hexahydrate at calcination temperature of 450 °C. The EDX spectrum showed the presence of zinc with a weight percent of 30.86 %, oxygen with a weight percent of 27.80 % and carbon with a weight percent of 41.34 %.

Figure 4.4.22(C) presents the EDX profile of zinc oxide nanoparticles synthesised using 15 g of zinc nitrate hexahydrate at calcination temperature of 450 °C. The EDX spectrum showed the presence of zinc with a weight percent of 33.01 %, oxygen with a weight percent of 21.96 % and carbon with a weight percent of 45.02 %.

Figure 4.4.22(D) presents the EDX profile of zinc oxide nanoparticles synthesised using 20 g of zinc nitrate hexahydrate at calcination temperature of 450 °C. The EDX spectrum showed the presence of zinc with a weight percent of 24.27 %, oxygen with a weight percent of 22.91 % and carbon with a weight percent of 52.82 %.

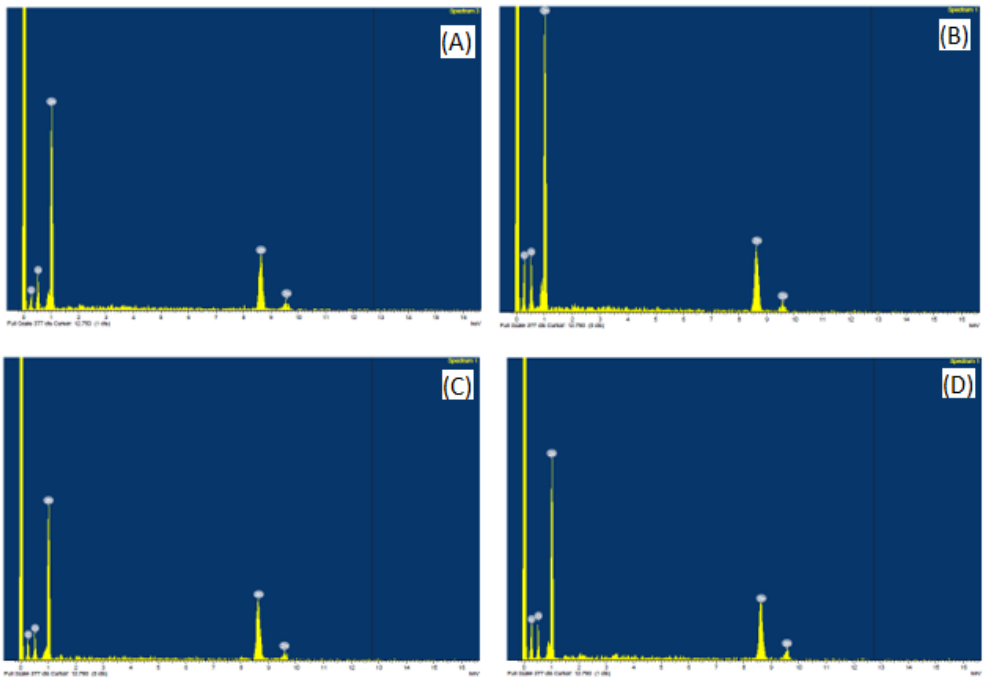

Figure 4.4.22: EDX profiles of ZnO NPs synthesised using (A) 5 g, (B) 10 g, (C) 15 g and (D) 20 g of $Zn(NO_3)_2.6H_2O$ at 450 °C

Figure 4.4.23(A) presents the EDX profile of zinc oxide nanoparticles synthesised using 5 g of zinc nitrate hexahydrate at calcination temperature of 550 °C. The EDX spectrum showed the presence of zinc with a weight percent of 48.28 %, oxygen with a weight percent of 23.93 % and carbon with a weight percent of 27.79 %.

Figure 4.4.23(B) presents the EDX profile of zinc oxide nanoparticles synthesised using 5 g of zinc nitrate hexahydrate at calcination temperature of 650 °C. The EDX spectrum showed the presence of zinc with a weight percent of 39.07 %, oxygen with a weight percent of 28.16 % and carbon with a weight percent of 32.77 %.

Figure 4.4.23(C) presents the EDX profile of zinc oxide nanoparticles synthesised using 5 g of zinc nitrate hexahydrate at calcination temperature of 750 °C. The EDX spectrum showed the presence of zinc with a weight percent of 65.48 % and oxygen with a weight percent of 34.52 %. Only Zn and O existed in the nanoparticles, hence indicating that the nanoparticles synthesized was pure and free from impurities.

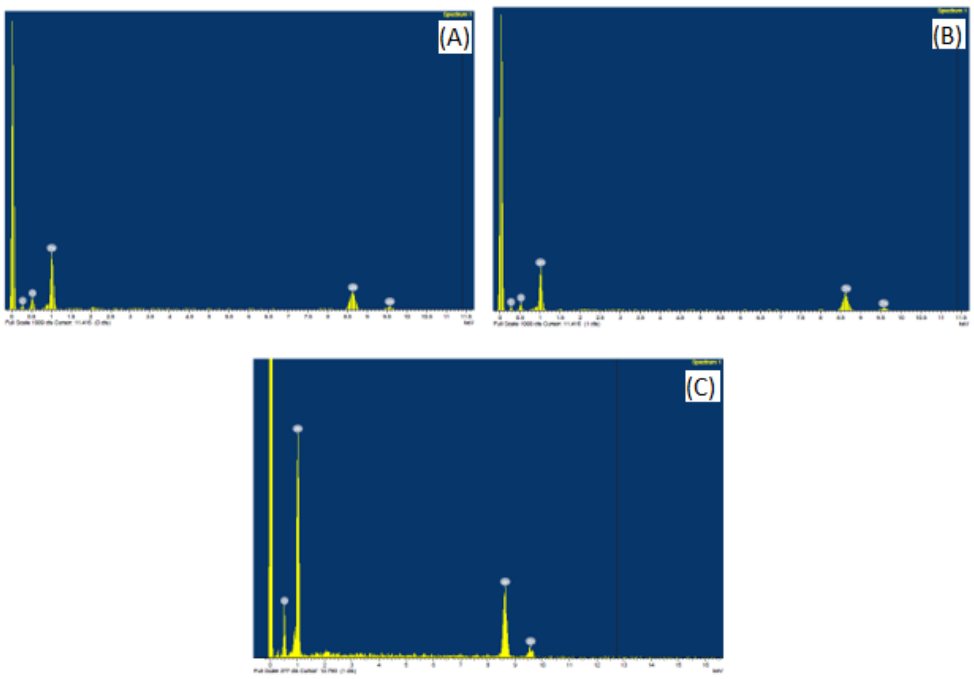

Figure 4.4.23: EDX profiles of ZnO NPs synthesised using 5 g of $Zn(NO_3)_2.6H_2O$ at (A) 550 °C, (B) 650 °C and (C) 750 °C

The presence of Zn and O in all the EDX spectra proved the formation of zinc oxide. The peak at 0 keV is the noise peak or so called zero energy strobe peak (Boothroyd, 2010). This noise peak serves as a reference peak corresponding to zero energy (Statham, 2002). Often, threshold settings are revised to reduce the zero-energy peak.

From the EDX spectra obtained, it had shown that carbon also existed in the zinc oxide nanoparticles synthesised. This might be due to the adhesion of phytochemicals in the peppermint tea dregs extract on the nanoparticles synthesised. Another possible source was from the carbon tape that used to attach the sample on the stand. In addition, the surface of the samples might be

deposited with carbon coating during the preparation of samples for the EDX analysis (Vac Coat, 2020). Since carbon is ubiquitous in real samples, the K-peaks frequently obstruct with the detection of L- and M-peaks for a wide range of elements. Thus, whether using a peak identification approach that is either automated or manual, having access to the greater levels of energy K-shell and L-shell peaks with more than 5 keV photon energy considerably enhances the opportunity of detecting elements with intermediate and high atomic number (Newbury, 2007).

Nevertheless, in general, the weight percent of carbon decreased when the calcination temperature increased. This served as an evidence that carbon compounds would be thermally decomposed at higher temperatures.

4.4.6 Particle Size Analysis (PSA)

The particle size distribution (PSD) of zinc oxide nanoparticles was determined by particle size analyser (PSA). The particle size analyser determines the particle size using the concept of light scattering of particles with the aid of refractive index.

Figure 4.4.24 presents the particle size distributions of zinc oxide nanoparticles synthesised using 5 g, 10 g, 15 g and 20 g of zinc nitrate hexahydrate at 450 °C calcination temperature. The average particle size obtained were 33.550 μm, 39.866 μm, 40.179 μm and 48.843 μm respectively.

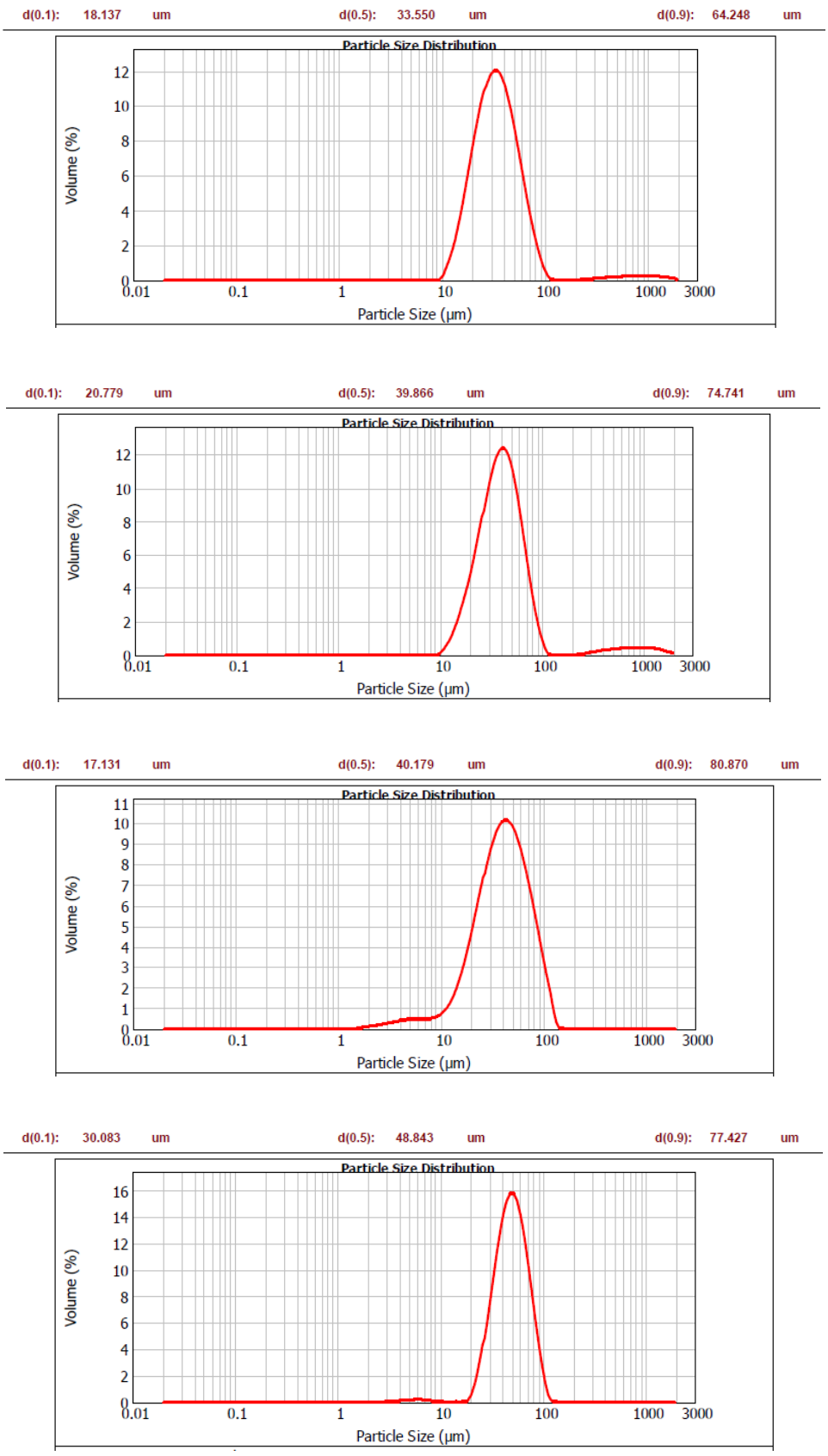

Figure 4.4.24: PSD of ZnO NPs synthesised using (A) 5 g, (B) 10 g, (C) 15 g and (D) 20 g of $Zn(NO_3)_2.6H_2O$ at 450 °C

Figure 4.4.25 presents the particle size distributions of zinc oxide nanoparticles synthesised using 5 g of zinc nitrate hexahydrate at 550 °C, 650 °C and 750 °C calcination temperature. The average particle size obtained was 34.417 µm, 31.578 µm and 42.709 µm respectively.

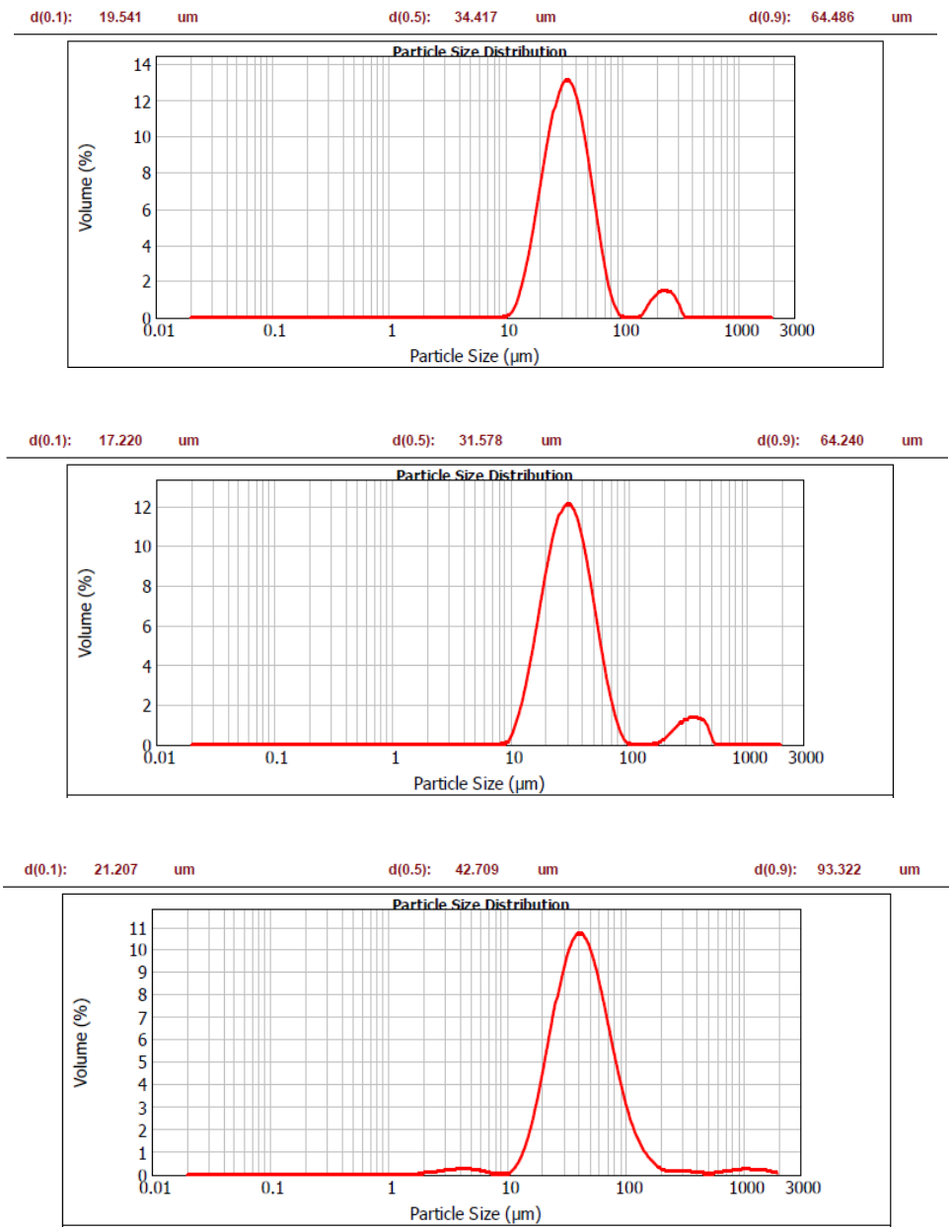

Figure 4.4.25: PSD of ZnO NPs synthesised using 5 g of $Zn(NO_3)_2.6H_2O$ at (A) 550 °C, (B) 650 °C and (C) 750 °C

According to the findings, the particle sizes obtained in this analysis did not match with the particle sizes obtained in FESEM nor did it fit in term of size of nanoparticles. This was due to the agglomeration of synthesized zinc oxide nanoparticles, as seen in FESEM images. The agglomeration of particles occurred as there was no alkaloid present in the peppermint tea dregs extract which functions as a capping agent that prevent agglomeration of nanoparticles, as proven in qualitative phytochemical screening of crude extract.

Generally, the particle size still increased with increasing mass of zinc nitrate hexahydrate and increasing calcination temperature, as revealed in other characterisation methods as well. However, these results could not be used as the only indicator because the particle sizes obtained were the outcomes of particle agglomeration.

4.5 Photocatalytic Performance of Zinc Oxide Nanoparticles

The photocatalytic performance of zinc oxide nanoparticles synthesised using 5 g of zinc nitrate hexahydrate at 450 °C was evaluated by the degradation of crystal violet dye solution with exposure to sunlight. This particular ZnO NPs was selected as it had the smallest particle size which effectively increased the surface area over volume ratio of the nanoparticles to be acted as a photocatalyst.

Prior to illumination, the crystal violet dye solutions were allowed to stir constantly in dark for 30 minutes to obtain equilibrium of adsorption and desorption between dye molecules and ZnO NPs photocatalyst. The extent of crystal violet dye degradation by ZnO NPs photocatalyst was monitored by using UV-visible spectroscopy. The maximum absorption wavelength of crystal violet dye was determined as 583 nm. Hence, 583 nm was set to measure the absorbance of crystal violet dye at regular time intervals. Using Equation 3.5, the percentage of dye degradation was calculated on the basis of the absorbances measured.

To determine the effectiveness of ZnO NPs photocatalyst, the degradation of crystal violet dye was done under different conditions. Table 4.5.1 and Figure 4.5.1 present the efficiency of crystal violet dye photodegradation under various conditions. Beer-Lambert law asserts that the absorbance and concentration of a sample have a linear relationship. The higher the concentration, the higher the absorbance. Therefore, lower absorbance value obtained indicated that the concentration of crystal violet dye was lower, which was the consequence of crystal violet dye degradation.

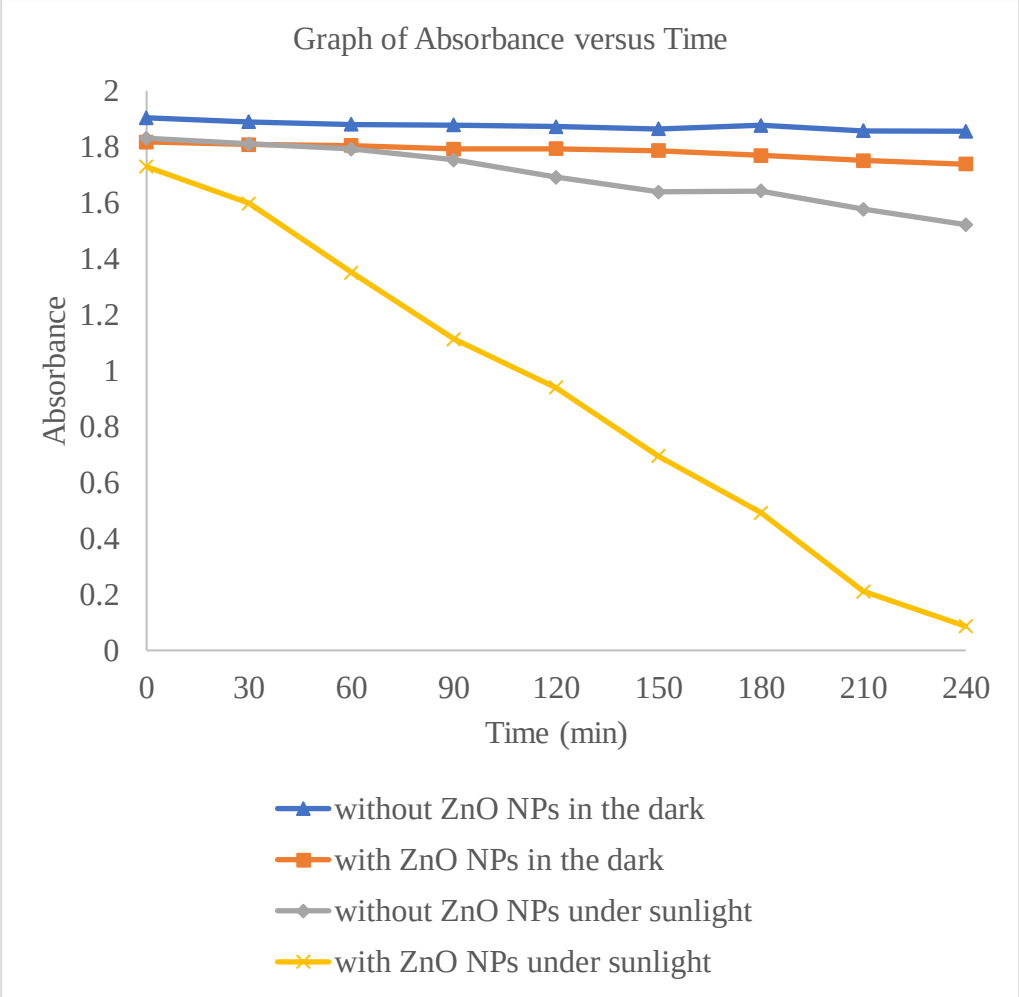

Figure 4.5.1: Graph of absorbance versus time for crystal violet dye degradation under various conditions

By comparison, the crystal violet showed lower absorbance value with ZnO NPs than those without ZnO NPs at the beginning. This was due to the adsorption of nanoparticles on the surface of crystal violet dye.

Based on Figure 4.5.1, in the absence of ZnO NPs or sunlight or both, the crystal violet dye showed negligible degradation. For the photodegradation of CV dye with the help of ZnO NPs, the intensity of the absorption at λ_{max}

decreased substantially as time gone from 0 to 240 minutes, indicating that the percentage of photodegradation increased over time. Within 4 hours of exposure to sunlight, the percentage of photodegradation of crystal violet dye was 95.03 % as presented in Figure 4.5.2.

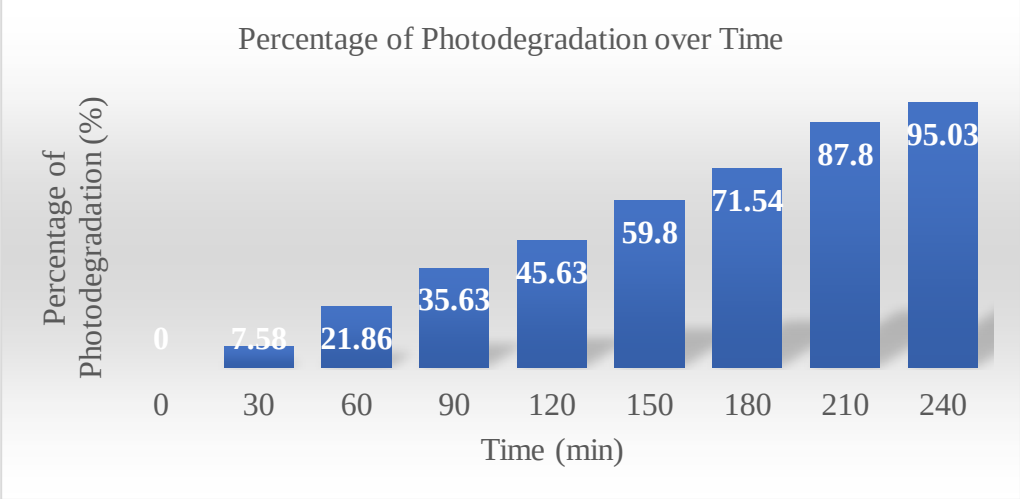

Figure 4.5.2: Bar graph of percentage of photodegradation of crystal violet dye under sunlight over time

Based on Table 4.5.1, it was clear that crystal violet dye degraded fastest in the presence of ZnO NPs photocatalyst and sun irradiation. As a result, ZnO NPs acted as a good photocatalyst in photodegradation of crystal violet dye.

Table 4.5.1: Percentage of photodegradation of crystal violet dye under various conditions

Beaker	Photocatalyst (ZnO NPs)		Condition		Percentage of dye degradation at 240th minute
	With	Without	In the dark	Under sunlight	
A		✓	✓		2.52 %
B	✓		✓		4.40 %
C		✓		✓	16.88 %
D	✓			✓	95.03 %

Figure 4.5.3 shows the molecular structure of crystal violet.

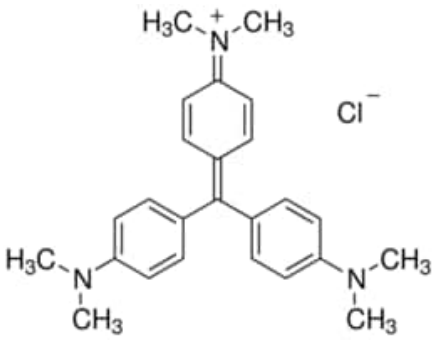

Figure 4.5.3: Molecular structure of crystal violet (Merck, 2022)

Principally, the hydroxyl radical (OH•) generated from the photocatalysis of ZnO NPs initiated the degradation process. It would first attack the weakest

bond at the centre of crystal violet structure and subsequently generate other possible products as shown in Appendix B. ZnO NPs captured a wide range of solar energy that was equal to or higher than its band gap energy, creating electron-hole pairs that led to the production of reactive radicals. Therefore, increased concentration of radicals formed by ZnO NPs increased the rate of photodegradation.

CHAPTER 5

CONCLUSIONS AND SUGGESTIONS

5.1 Conclusions

Zinc oxide nanoparticles had been successfully synthesised using peppermint tea (*Mentha piperita*) dregs extract and zinc nitrate hexahydrate as the metal precursor via a greener synthetic pathway.

Based on the results obtained from qualitative phytochemical screening, the bioactive compounds that present in the peppermint tea dregs extract was flavonoids which acted as the reducing agent and stabilising agent while alkaloids, saponins, tannins, proteins and glycosides were absent in the extract. Moreover, it was deduced that the percent yield of zinc oxide nanoparticles synthesised would not be affected by the mass of zinc nitrate hexahydrate and calcination temperature.

From the characterisation of zinc oxide nanoparticles synthesised by Fourier transform infrared spectroscopy (FTIR), ultraviolet-visible spectroscopy (UV-Vis), X-ray diffraction (XRD), field emission scanning electron microscopy (FESEM), energy dispersive X-ray analysis (EDX) and particle size analysis (PSA), it was concluded that the zinc oxide nanoparticles synthesised using 5 g of zinc nitrate hexahydrate at 450 °C calcination temperature was the best among all.

From its FTIR spectrum, the intense peak generated at around 449 cm^{-1} implied the Zn-O stretching vibration. Its UV-Vis spectrum also showed a maximum absorption wavelength at 368 nm, hence having a band gap energy of 3.37 eV. Additionally, XRD analysis revealed that the relative pattern of the synthesized zinc oxide nanoparticles was 93.9 % matched with ICDD 01-070-2551 with hexagonal wurtzite structure. By using the Debye-Scherrer's equation, the average crystallite size was calculated to be 47.23 nm. From the FESEM image, it could be observed that the agglomerated particles synthesised were irregularly shaped spherical with a dimension ranging from 20.0 nm to 35.0 nm. The EDX spectrum showed the presence of zinc with a weight percent of 40.92 %, oxygen with a weight percent of 25.68 % and carbon with a weight percent of 33.40 %. Other than that, the average particle size obtained from PSA was 33.550 μm but this dimension was due to agglomeration of the particles resulted from the absence of alkaloids in the peppermint tea dregs extract.

Last but not least, the zinc oxide nanoparticles showed excellent photocatalytic performance as it obtained a 95.03 % photodegradation of crystal violet dye within 4 hours of exposure to sunlight. In conclusion, the synthesised zinc oxide nanoparticles acted as a good photocatalyst in the photodegradation of crystal violet dye and may find potential applications in industrial wastewater treatment.

5.2 Suggestions for Further Work

First and foremost, different types of agricultural waste can be used to synthesise zinc oxide nanoparticles to find out the best raw materials to be used. Quantitative analysis of phytochemicals can be carried out to determine the effect of amount of phytochemicals on the nanoparticles synthesized. Apart from that, TEM is preferred for the average size distribution of the nanoparticles synthesized for better clarification. Besides, the photodegradation of crystal violet dye can be further analysed by FTIR spectroscopy to identify the functional groups of the dye that interacted with zinc oxide nanoparticles. The intermediate products of degradation can be characterised using GC-MS and LC-MS to propose a mechanism for the degradation pathway.

REFERENCES

Adelere, I.A. and Lateef, A., 2016. A Novel Approach to the green Synthesis of Metallic Nanoparticles: the Use of Agro-Wastes, Enzymes, and Pigments. *Nanotechnology Rev,* 5(6), pp. 567-587.

Ahmad, R.A.R. et al., 2019. Biosynthesis of zinc oxide nanoparticles by using fruits extracts of Ananas comosusand its antibacterial activity. *Malaysian Journal of Fundamental and Applied Sciences,* 15(2), pp. 268-273.

Ajmal, A., Majeed, I., Malik, R.N., Idriss, H. and Nadeem, M.A., 2014. Principles and mechanisms of photocatalytic dye degradation on TiO_2 based photocatalysts: a comparative overview. *RSC Advances,* 4(70), pp. 37003-37026.

Ameta, R., Solanki, M.S., Benjamin, S. and Ameta, S.C., 2018. Photocatalysis. In: *Advanced Oxidation Processes for Waste Water Treatment.* London: Elsevier, pp. 135-175.

Aminuzzaman, M. et al., 2019. Value-adding to dragon fruit (*Hylocereus polyrhizus*) peel biowaste: green synthesis of ZnO nanoparticles and their characterization. *Inorganic and Nano-Metal Chemistry,* 49(11), pp. 401-411.

Bacaksiz, E. et al., 2008. The effects of zinc nitrate, zinc acetate and zinc chloride precursors on investigation of structural and optical properties of ZnO thin films. *Journal of Alloys and Compounds,* 466(1-2), pp. 447-450.

Banu, K.S. and Cathrine, L., 2015. General Techniques Involved in Phytochemical Analysis. *International Journal of Advanced Research in Chemical Science (IJARCS),* 2(4), pp. 25-32.

Bhatia, S. and Devraj, S., 2017. *Pollution Control in Textile Industry.* 1st ed. New York: WPI Publishing.

Boothroyd, C.B., 2010. *X-Ray Analysis.* Technical University of Denmark.

Bronzino, J., 2005. 15 - RADIATION IMAGING. In: Enderle, J.D., Blanchard, S.M. and Bronzino, J.D. (eds.). *Introduction to Biomedical Engineering.* 2nd ed. New York: Academic Press, pp. 857-904.

Chauhan, R.P.S., Gupta, C. and Prakash, D., 2012. Methodological advancements in green nanotechnology and their applications in biological synthesis of herbal nanoparticles. *International Journal of Bioassays,* 1(7), pp. 6-10.

Din, M.I. et al., 2021. Biofabrication of Size-Controlled ZnO Nanoparticles Using Various Capping Agents and Their Cytotoxic and Antitermite Activity. *Journal of Environmental Analytical Chemistry,* 101(6), pp. 821-837.

Dobson, R.S. and Burgess, J.E., 2007. Biological treatment of precious metal refinery wastewater: A review. *Minerals Engineering,* 20(6), pp. 519-532.

Fatimah, I., 2018. Biosynthesis and Characterization of ZnO Nanoparticles using Rice Bran Extract as Low-Cost Templating Agent. *Journal of Engineering Science and Technology,* 13(2), pp. 409-420.

Gibson, P. and Holzwarth, U., 2011. The Scherrer equation versus the 'Debye–Scherrer equation'. *NATURE NANOTECHNOLOGY,* 6(9), p. 534.

Gour, A. and Jain, N.K., 2019. Advances in green synthesis of nanoparticles. *Artificial cells, Nanomedicine, and Biotechnology,* 47(1), pp. 844-851.

Grigoleit, H.G. and Grigoleit, P., 2005. Peppermint oil in irritable bowel syndrome. *Phytomedicine,* 12(8), pp. 601-606.

Gupta, A. et al., 2015. Comparison of physical and electrochemical properties of ZnO prepared via different surfactant-assisted precipitation routes. *Applied Nanoscience,* 5(7), pp. 787-794.

Hicks, A., 2009. Current status and future development of global tea production and tea products. *Assumption University Journal of Technology,* 12(4), pp. 251-264.

Honsberg, C. and Bowden, S., 2022. *Band Gap*. [Online] Available at: https://www.pveducation.org/pvcdrom/pn-junctions/band-gap#:~:text=The%20band%20gap%20(EG,for%20electrons%20in%20a%20solid. [Accessed 15 April 2022].

Hossain, M.A. et al., 2013. Study of total phenol, flavonoids contents and phytochemical screening of various leaves crude extracts of locally grown Thymus vulgaris. *Asian Pacific Journal of Tropical Biomedicine,* 3(9), pp. 705-710.

Hussain, I. et al., 2016. Green synthesis of nanoparticles and its potential application. *Biotechnology Letters,* 38, pp. 545-560.

Isai, K.A. and Shrivastava, V.S., 2019. Photocatalytic degradation of methylene blue using ZnO and 2% Fe–ZnO semiconductor nanomaterials synthesized by sol–gel method: a comparative study. *SN Applied Sciences,* 1.

Jiang, Y.R. et al., 2015. Controlled hydrothermal synthesis of BiOxCly/BiOmIn composites exhibiting visible-light photocatalytic degradation of crystal violet. *Journal of Hazardous Materials,* 283, pp. 787-805.

Joerger, R., Klaus, T. and Granqvist, C.G., 2000. Biologically produced silver carbon composite materials for optically functional thin-film coatings. *Advanced Materials,* 12(6), pp. 407-409.

Kamineni, S., Manepally, M. and Kamineni, E.P., 2016. Musculoskeletal ProteinAnalysis Techniques - A Review. *Journal of Rheumatology and Arthritic Diseases,* 1(2), pp. 1-9.

Kapp, K. et al., 2013. Commercial peppermint (Mentha × piperita L.) teas: Antichlamydial effect and polyphenolic composition. *Food Research International,* 53, pp. 758-766.

Kargozar, S. and Mozafari, M., 2018. Nanotechnology and Nanomedicine: Start small, think big. *Material Today: Proceedings,* 5(7), pp. 15592-15500.

Karimi, L., Zohoori, S. and Yazdanshenas, M.E., 2014. Photocatalytic degradation of azo dyes in aqueous solutions under UV irradiation using nano-strontium titanate as the nanophotocatalyst. *Journal of Saudi Chemical Society,* 18(5), pp. 581-588.

Khan, I., Saeed, K. and Khan, I., 2017. Nanoparticles: Properties, applications and toxicities. *Arabian Journal of Chemistry.*

Kołodziejczak-Radzimska, A. and Jesionowski, T., 2014. Zinc Oxide—From Synthesis to Application: A Review. *Materials,* 7(4), pp. 2833-2881.

Kulkarni, P., Sureshkumar, R. and Biswas, P., 2003. Multiscale simulation of irreversible deposition in presence of double layer interactions. *Journal of Colloid and Interface Science*, 260(1), pp. 36-48.

Leon, L., Chung, E.J. and Rinaldi, C., 2020. A brief history of nanotechnology and introduction to nanoparticles for biomedical application. Nanoparticles for Biomedical Application. In: *Nanoparticles for Biomedical Applications.* London: Elsevier, pp. 1-4.

McKay, D.L. and Blumberg, J.B., 2006. A review of the bioactivity and potential health benefits of peppermint tea (*Mentha piperita L.*). *Phytotherapy Research,* 20, pp. 619-633.

Merck, 2022. *Crystal Violet.* [Online] Available at: https://www.sigmaaldrich.com/MY/en/substance/crystalviolet40798548629 [Accessed 17 April 2022].

Messing, G.L., 2021. Calcination and Phase Transformations. In: Pomeroy, M. (ed.). *Encyclopedia of Materials: Technical Ceramics and Glasses.* PA: Elsevier, pp. 83-92.

Miah, M.I., 2021. Size- and temperature-control optical direct/indirect band tuning in layered compounds: band gap engineering. *Optical and Quantum Electronics,* 53(618).

Mishra, V., Balomajumder, C. and Agarwal, V., 2010. Biosorption of Zn (II) onto the Surface of Non-living Biomasses: A Comparative Study of Adsorbent Particle Size and Removal Capacity of Three Different Biomasses. *Water, Air & Soil Pollution*, 211, pp. 489-500.

Mohamed, W.A.A. et al., 2021. Quantum dots synthetization and future prospect applications. *Nanotechnology Reviews*, 10(1), pp. 1926-1940.

Mohammadian, M., Es'haghi, Z. and Hooshmand, S., 2018. Green and chemical synthesis of zinc oxide nanoparticles and size evaluation by UV–vis spectroscopy. *Journal of Nanomedicine Research*, 7(1), pp. 52-58.

Muruganandham, M., Chen, I.S. and Wu, J.J., 2009. Effect of temperature on the formation of macroporous ZnO bundles and its application in photocatalysis. *Journal of Hazardous Materials*, 172, pp. 700-706.

Nadaroğlu, H., Alayli G*ü*ng*ö*r, A. and *İnce*, S., 2017. Synthesis of Nanoparticles by Green Synthesis Method. *International Journal of Innovative Research and Review*, 1(1), pp. 6-9.

Nasrollahzadeh, M., Sajad, S.M., Sajjadi, M. and Issaabadi, Z., 2019. An Introduction to Nanotechnology. *Interface Science and Technology*, 28, pp. 1-27.

Nawaz, H.R., Solangi, B.A., Zehra, B. and Nadeem, U., 2011. Preparation of Nano Zinc Oxide and its Application inLeather as a Retanning and Antibacterial Agent. *Canadian Journal on Scientific and Industrial Research*, 2(4), pp. 164-170.

Newbury, D.E., 2007. Mistakes Encountered during Automatic Peak Identification in Low Beam Energy X-ray Microanalysis. *Scanning*, 29, pp. 137-151.

Opoku, F., Govender, K.K., Sittert, C.G.C.E. and Govender, P.P., 2017. Understanding the mechanism of enhancedcharge separation and visible light photocatalyticactivity of modified wurtzite ZnO withnanoclusters of ZnS and graphene oxide:from a hybrid density functional study. *New Journal of Chemistry* , 41(16), pp. 8140-8155.

Orts, F. et al., 2018. Electrochemical treatment of real textile wastewater: Trichromy Procion HEXL®. *Journal of Electroanalytical Chemistry,* 808, pp. 387-394.

Patra, J.K. and Baek, K.H., 2014. Green Nanobiotechnology: Factors Affecting Synthesis and Characterization Techniques. *Journal of Nanomaterials,* pp. 1-12.

Peixoto, I.T.A. et al., 2009. Potential pharmacological and toxicological basis of the essential oil from Mentha spp. *Journal of the Basic and Applied Pharmaceutical Sciences,* 30(3), pp. 235-239.

Prabhu, S. and Poulose, E.K., 2012. Silver nanoparticles: mechanism of antimicrobial action, synthesis, medical applications, and toxicity effects. *International Nano Letters 2,* 32.

Rita, P. and Animesh, K., 2011. An updated overview on peppermint (*Mentha piperita*). *International Research Journal of Pharmacy,* 2(8), pp. 1-10.

Saravanan, R. et al., 2013. The photocatalytic activity of ZnO prepared by simple thermal decomposition method at various temperatures. *Journal of Molecular Liquids,* 177, pp. 394-401.

Shaheen, I. and Ahmad, K.S., 2020. Chromatographic Identification of "green Capping Agents" Extracted from *Nasturtium Officinale (Brassicaceae)* Leaves for the Synthesis of MoO_3 Nanoparticles. *Journal of Separation Science,* 43(3), pp. 598-605.

Shah, M. et al., 2015. Green Synthesis of Metallic Nanoparticles via Biological Entities. *Materials,* 8(11), pp. 7278-7308.

Sheel, R., Nisha, K. and Kumar, J., 2014. Preliminary Phytochemical Screening of Methanolic Extract Of Clerodendron infortunatum. *Journal of Applied Chemistry,* 7(1), pp. 10-13.

Shkurupii, V.A., Odintsova, O.A. and Kazarinova, N.V., 2006. Use of essential of peppermint (*Mentha piperita*) in the complex treatment of patients with infiltrative pulmonary tuberculosis. *Problemy Tuberkuleza i Bolezneĭ Legkikh,* 9, pp. 43-45.

Statham, P.J., 2002. Limitations to Accuracy in Extracting Characteristic Line Intensities From X-Ray Spectra. *Journal of Research of the National Institute of Standards and Technology,* 107(6), pp. 531-546.

Sulaiman, C.T. and Balachandran, I., 2012. Total Phenolics and Total Flavonoids in Selected Indian Medicinal Plants. *Indian Journal of Pharmaceutical Sciences,* 74(3), pp. 258-260.

Thakkar, K.N., Mhatre, S.S. and Parikh, R.Y., 2010. Biological synthesis of metallic nanoparticles. *Nanomedicine: Nanotechnology, Biology, and Medicine,* 6, pp. 257-262.

Tugiyanti, E., Susanti, E. and Sulistyawan, I.H., 2019. Effect of Tea Dregs Form and Different Fermentation Process on the Nutrient, Tannin, Saponin, flavonoid content and Antioxidant Activity. *Pakistan Journal of Nutrition,* 18(1), pp. 25-33.

Usman, H., Abdulrahman, F. and Usman, A., 2009. Qualitative Phytochemical Screening and In Vitro Antimicrobial Effects of Methanol Stem Bark Extract of *Ficus Thonningii* (*Moraceae*). *African Journal of Traditional, Complementary and Alternative Medicines: AJTCAM,* 6(3), pp. 289-295.

Vac Coat, 2020. *CARBON COATING FOR EM AND EDX SAMPLE PREPARATION.* [Online] Available at: https://vaccoat.com/blog/carbon-coating-for-em-edx-sample-preparation/ [Accessed 16 April 2022].

Wang, J. et al., 2005. Synthesis and characterization of multipod, flower-like, and shuttle-like ZnO frameworks in ionic liquids. *Materials Letters,* 59(11), pp. 1405-1408.

Wani, K.A., Jangid, N.K. and Bhat, A.R., 2019. *Impact of textile dyes on public health and the environment.* United States of America: IGI Global.

Zheng, Y. et al., 2015. Green biosynthesis and characterization of zinc oxide nanoparticles using Corymbia citriodora leaf extract and their photocatalytic activity. *Green Chemistry Letters and Reviews,* 8(2), pp. 59-63.

APPENDIX A

Different Approaches and Methods for Synthesis of Nanoparticles

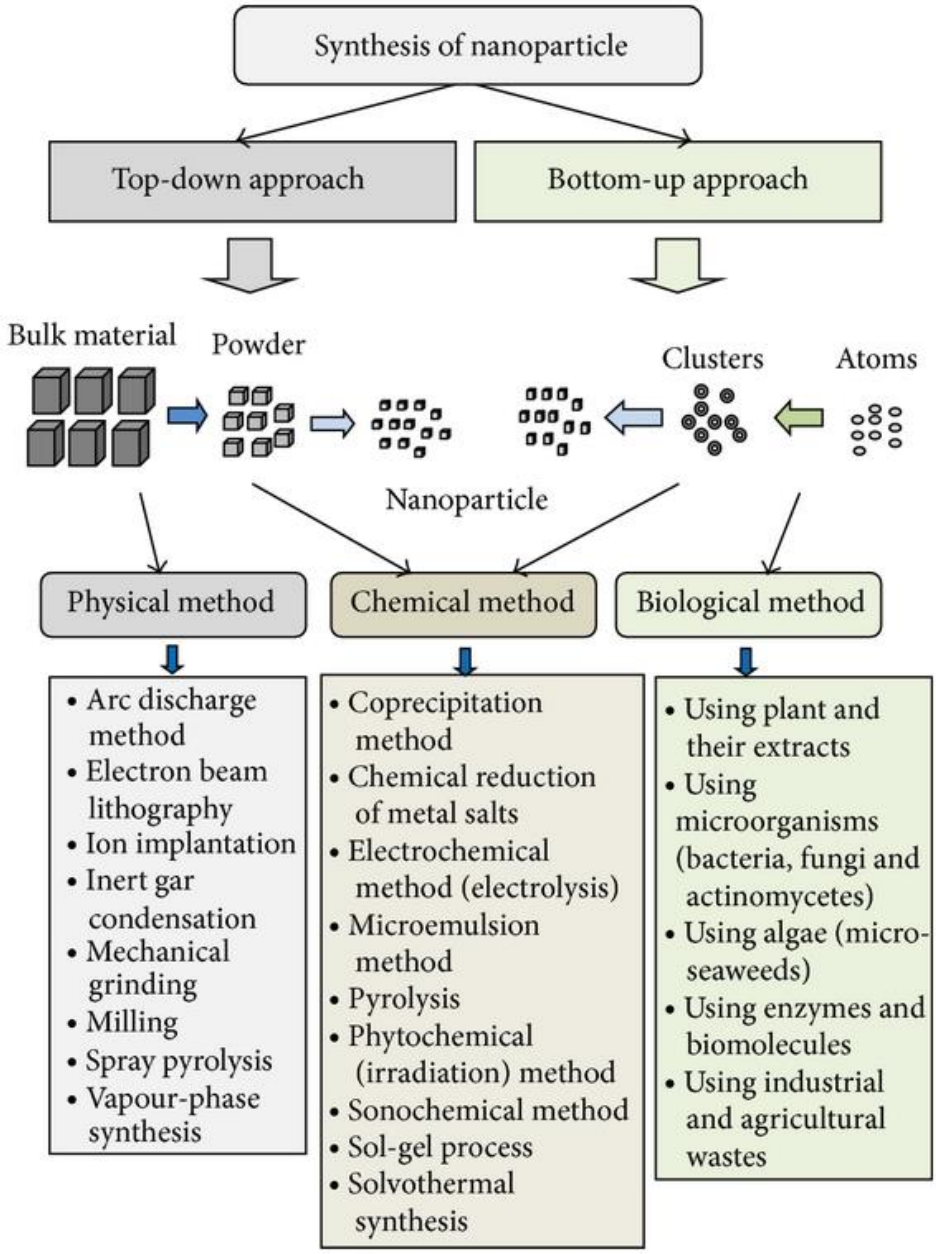

(Patra and Baek, 2014)

APPENDIX B

Possible Oxidation Degradation Mechanism of Crystal Violet Dye

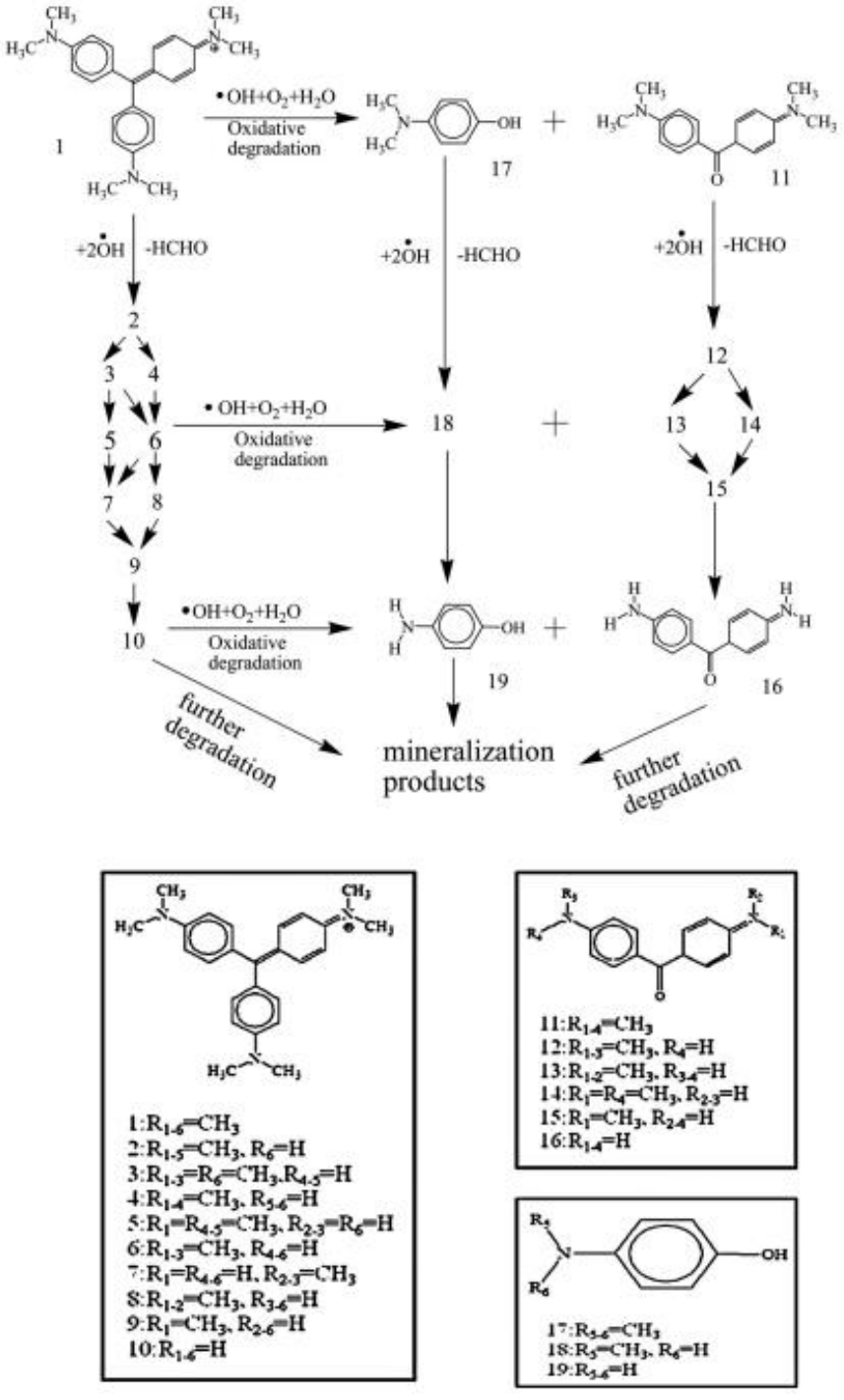

(Jiang, et al., 2015)